Analysis and Improvement of Large-Disturbance Stability for Grid-Connected VSG Based on Output Impedance Optimization

Mingxuan Li, *Member, IEEE*, Sirui Shu, Yue Wang, *Member, IEEE*, Peng Yu, Yonghui Liu, *Member, IEEE*,
Zhenyuan Zhang, *Senior Member, IEEE*, Weihao Hu, *Senior Member, IEEE*,
and Frede Blaabjerg, *Fellow, IEEE*

***Abstract*—Except for the benefits of mimicking synchronous generators, virtual synchronous generators (VSGs) still face particular small- and large-disturbance stability problems in practical applications. Therein, the large-disturbance stability is a much more dramatic and intractable problem, such as a short circuit or line tripping. Accordingly, this article explores this challenging problem from the perspective of output impedance optimization for VSGs. First, focusing on the potential risk of overcurrent during the electromagnetic process, the dynamic performances of different virtual impedance control structures used in VSGs are comparatively analyzed, and the output impedance boundary for suppressing the transient current is derived. Then, the output impedance boundaries for maintaining electromechanical transient stability are discussed in depth by using Lyapunov stability theory, which provides novel virtual impedance optimal design guidelines exclusively for the large-disturbance stability. Furthermore, a large-disturbance stability enhancement strategy based on adaptive virtual impedance control is proposed, which can limit the electromagnetic transient current and improves the electromechanical transient stability simultaneously. Finally, experiments validate the accuracy of the theoretical analysis and the effectiveness of the proposed strategy.**

***Index Terms*—Grid-connected inverter, large-disturbance stability, transient stability, virtual impedance, virtual synchronous generator (VSG).**

I. INTRODUCTION

With the rapid development of renewable energy, power electronic inverters have been more and more widely employed in the power system as the most typical grid-connected interfaces of renewable energy sources (RES) [1]. However, the traditional commonly used control strategies of grid-connected inverters, such as maximum power point tracking or constant power control, cannot provide inertia and damping, and support voltage or frequency for the power system, which may bring serious challenges to the stability of the power grid with high penetration of RES [2]. To handle this problem, the concept of virtual synchronous generator (VSG) is proposed and has become a promising technology, which equips the grid-connected inverters with the same external characteristics as the traditional synchronous generators (SGs) by mimicking the governor and the rotor swing equation [3], [4].

However, except for the benefits of resembling SGs, VSGs also face some particular stability problems in practical applications. Generally, these stability issues can be divided into small-disturbance stability and large-disturbance stability [5]. Substantial research has been devoted to the small-disturbance stability analysis, namely how a VSG responds to a small disturbance and remains the stable and continuous operation at some steady-state point. These articles commonly take the linear control theory, e.g., the root locus analysis or Nyquist criterion, as the mathematical tools, which are based on linear models built around some steady-state operating points [6]–[8]. However, from a stability point of view, VSGs also face large-disturbance stability problems, such as short circuits or line tripping, which are much more dramatic than small-disturbance stability issues and should be addressed more carefully. Because of neglecting the nonlinear characteristics, the commonly used small-disturbance stability analysis approaches cannot be applied to the analysis of large-disturbance stability directly [9]–[12].

Practically, when such a large disturbance occurs, high currents and large power imbalances will be seen. Therefore, proper actions should be taken quickly to limit the current and maintain stability [13]–[15]. This article will mainly focus on this

Manuscript received August 20, 2021; revised November 20, 2021 and January 23, 2022; accepted February 15, 2022. Date of publication February 23, 2022; date of current version April 28, 2022. This work was supported by the National Natural Science Foundation of China under Grant 51777159. Recommended for publication by Associate Editor A. Davoudi. *(Corresponding author: Yue Wang.)*

Mingxuan Li is with the School of Mechanical and Electrical Engineering, University of Electronic Science and Technology of China, Chengdu 611731, China, and also with the School of Electrical Engineering, Xi'an Jiaotong University, Xi'an 710049, China (e-mail: limx@uestc.edu.cn).

Sirui Shu, Yue Wang, and Peng Yu are with the School of Electrical Engineering, Xi'an Jiaotong University, Xi'an 710049, China (e-mail: ssr5dd@stu.xjtu.edu.cn; davidwangyue@mail.xjtu.edu.cn; tinyfish0203@stu.xjtu.edu.cn).

Yonghui Liu is with the School of Electrical Engineering, Xi'an Jiaotong University, Xi'an 710049, China, and also with the Department of Electrical Engineering, The Hong Kong Polytechnic University, 999077, Hong Kong (e-mail: liuyonghui@stu.xjtu.edu.cn).

Zhenyuan Zhang and Weihao Hu are with the School of Mechanical and Electrical Engineering, University of Electronic Science and Technology of China, Chengdu 611731, China (e-mail: zhangzhenyuan@uestc.edu.cn; whu@uestc.edu.cn).

Frede Blaabjerg is with the Department of Energy Technology, Aalborg Unviersity, 9220 Aalborg, Denmark (e-mail: fbl@et.aau.dk).

Color versions of one or more figures in this article are available at https://doi.org/10.1109/TPEL.2022.3153563.

Digital Object Identifier 10.1109/TPEL.2022.3153563

challenging problem, namely how a VSG behaves properly to maintain transient stability when it suffers from a large disturbance. The transient process under a large disturbance is usually divided into two parts according to their time scale, viz., electromagnetic transient process and electromechanical transient process [16]. Therein, the electromagnetic transient process refers to the fastest dynamics of VSGs immediately after the large disturbance appears, mainly including the transient responses of the voltage and current, where the frequency can be assumed constant because the system inertia prevents it from changing remarkably over this very short duration. The electromechanical transient process mainly refers to the swing dynamics of the power angle in a longer time scale, where the variation of the frequency and its interactions with the electromagnetic changes are considered further.

To address the adverse effects on electromagnetic transient responses caused by a large disturbance, various methods have been proposed. Compared with grid-following converters, the current limitation of grid-forming-based VSGs is a more intractable problem [12]. Mode-switching-based methods, which switch to grid-following control mode when a fault is detected, are often used to limit the fault current within the nominal range [14], [15]. Although these methods can suppress the overcurrent instantly, they are at a high risk of losing synchronization [11], [17]. Hardware-circuit-based methods, e.g., superconducting fault current limiters [18], are presented to restraint the current and disperse the superfluous energy of VSGs, which make a higher cost of the system. Model-predictive-control-based methods are also employed to prevent VSGs from overcurrent during a fault [19], [20], which greatly increase the complexity of the controllers. Virtual-impedance-based methods, viz. embedding a virtual impedance or resistance in the controller, are proven highly effective in limiting overcurrent [21]–[23], yet they only ensure a peak current limitation and seldom consider the dynamic response speed of current limiting. Moreover, the above methods lack the coordination between the electromagnetic current limitation and the electromechanical transient stability.

To tackle the nonlinear characteristics of the electromechanical transient response process, the equal area criterion method [24], [25] and phase portrait method [26]–[28] are adopted to analyze the transient stability of VSC. From the perspective of energy, the dynamic energy trajectory in the time domain is researched in [29], and Lyapunov's direct method is utilized in [30] to investigate the transient power angle stability of VSG. Compared with the time-domain methods, Lyapunov's direct method has the advantages of a simple calculation and great insights into the physical mechanism of stability. Moreover, the synchronization stability and frequency stability are improved by modifying the active power control in [31], and a mode-adaptive power angle stability enhancement method is proposed in [32]. The above research has made highly valuable contributions toward revealing the mechanism of electromechanical stability and enhancing the large-disturbance stability performance of VSGs. Nevertheless, the voltage and current transient response characteristics during the electromagnetic time scale are seldom considered together with the electromechanical stability carefully. Actually, the electromagnetic and electromechanical transient stability problems commonly contradict and restrict each other. How to coordinate them is a rather challenging and crucial problem, which should be given in-depth and overall consideration. Unfortunately, the existing literature has not involved such a thorough solution that can well address the electromagnetic and electromechanical transient stability problems of VSGs simultaneously. This is the main motivation and purpose of this article.

Compared with the existing research on the large-disturbance stability of VSGs, the contributions of this article are summarized into three aspects as follows. First, focusing on the electromagnetic transient process caused by a large disturbance, the dynamic characteristics of different virtual impedance control structures are comparatively analyzed, and then the output impedance boundaries for the current limitation are derived mathematically. The novel conclusions obtained here can help avoid the overcurrent more effectively over the electromagnetic transient process. Second, concerning the electromechanical transient process, the output impedance boundaries for maintaining power angle stability are further analyzed in depth by using Lyapunov stability theory, which provides novel virtual impedance design guidelines especially in terms of the large-disturbance stability issue. Third, from the perspective of adaptively optimizing the output impedance of VSG, a large-disturbance stability improvement strategy based on the foregoing theoretical analysis is proposed, which cannot only suppress the overcurrent more effectively but also enhance the frequency and power angle stability when a VSG suffers from a large disturbance.

The rest of this article is organized as follows. In Section II, the basic VSG control structure and large disturbance stability problem are introduced briefly. Then, an in-depth analysis of electromagnetic and electromechanical transient processes under a large disturbance is conducted in Sections III and IV, respectively. Moreover, a method to improve the large-disturbance stability of the VSG system is proposed in Section V. Experimental results are presented in Section VI. Finally, Section VII concludes this article.

II. Basic VSG Control Structure and Large-Disturbance Stability

The basic grid-connected VSG system is presented in Fig. 1 in which the RES is connected to the grid through a three-phase inverter controlled by a VSG algorithm. The VSG control involves two parts, which mimic the dynamic characteristics of the rotor swing and the governor in SGs, respectively, thereby enhancing the frequency supporting ability of RES.

First, P-ω droop control simulates the primary frequency regulation function of governor, which can be described by

$$P_m = P_{\text{ref}} - k_P\left(\omega - \omega_{\text{ref}}\right) \tag{1}$$

where P_m is the virtual mechanical power of droop control, k_P is the $P{-}\omega$ droop coefficient, ω is the angular frequency of the VSG output voltage, and ω_{ref} is the nominal angular frequency.

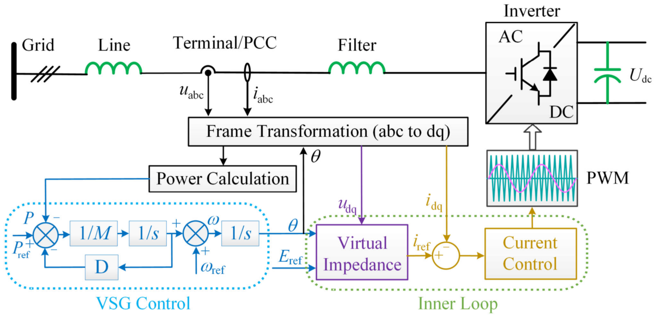

Fig. 1. Main circuit and control structure diagram of a grid-connected virtual synchronous generator (VSG) system.

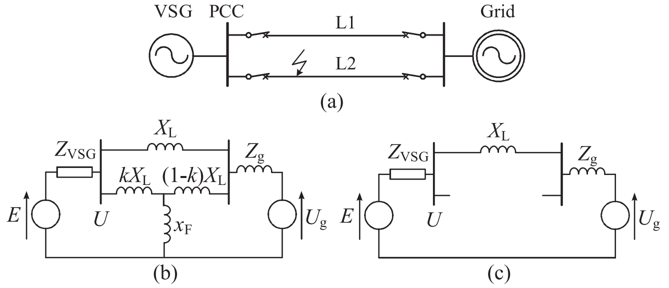

Fig. 2. Examples of large disturbances. (a) Schematic diagram of a VSG connected to the power grid through double-circuit transmission lines. (b) Equivalent circuit of a short circuit. (c) Equivalent circuit of a line tripping.

Then, a virtual inertia control is added to simulate the rotor swing equation of SGs, which is expressed mathematically as

$$M\frac{\mathrm{d}\omega}{\mathrm{d}t} = P_m - P - K_d\left(\omega - \omega_{\mathrm{ref}}\right) \tag{2}$$

where P is the output active power, M is the inertial coefficient and satisfies $M = J\omega_{\mathrm{ref}}$, J is the virtual moment of inertia, and K_d is the damping coefficient.

Combining (1) and (2) yields the complete VSG control. Meanwhile, considering k_P and K_d play the same role in the control loop, the whole VSG control can be expressed as

$$M\frac{\mathrm{d}\omega}{\mathrm{d}t} = P_{\mathrm{ref}} - P - D\left(\omega - \omega_{\mathrm{ref}}\right) \tag{3}$$

where D is the equivalent damping factor, $D = k_P + K_d$.

The VSG control generates the phase reference of inner potential, and further constitutes the voltage reference for the inner loop together with the amplitude reference E_{ref}. The inner loop controller involves voltage, current, and virtual impedance control to enhance the control performance. The inner loop is realized in *d*-*q* frame, where the *d*-axis is aligned to the phase of the inner potential of the VSG. Generally, the voltage amplitude reference E_{ref} can be tuned by various reactive power or voltage control methods, e.g., constant voltage control [25], constant reactive power control [33], *Q*-*V* droop control [34], inertia control [35], etc. Although the reactive power or voltage control structures can also exert an influence on the large-disturbance stability of the VSG system, the selection of the reactive power or voltage control structure does not affect the idea of this article. For the sake of simplicity and the limitation of space, only the constant voltage control as shown in Fig. 1 is analyzed in this article. Actually, the idea of this article can also be transplanted to other reactive power or voltage control structures easily.

The grid-connected VSG based on the above amplitude-phase control principle belongs to the family of grid-forming converters and can be regarded as a controlled voltage source [36]. Accordingly, both the VSG and the power grid can be equivalent to an ideal voltage source in series with an impedance, which can be indicated by E and Z_{VSG}, U_{g} and Z_{g}, respectively. Fig. 2(a) depicts a schematic diagram of a VSG connected to the power grid through double-circuit transmission lines $L1$ and $L2$. When a large disturbance, taking short circuit and line tripping for examples, appears somewhere on the line $L2$, the equivalent circuit diagrams can be drawn in Fig. 2(b) and (c), respectively. Therein, X_L is the equivalent reactance of the transmission line, k is a proportional coefficient satisfying $k \in [0,\ 1]$, and x_F is the shunt impedance, which has different values for different types of large disturbances, and especially $x_F = 0$ represents a three-phase short circuit [16]. For any other disturbances, e.g., generators or loads switching, etc., and other connection structures, e.g., single-circuit connection, etc., the equivalent circuits can also be drawn similarly. It can be concluded that no matter which type of large disturbance occurs on the grid, the terminal voltage of the VSG will change following the large disturbance. Consequently, the power angle characteristics of the VSG will thereupon alter. Particularly, in some serious cases, e.g., the three-phase short circuit, the terminal voltage can plummet severely and then would incur overcurrent and power angle instability problems in quick succession.

Based on the above analysis, regardless of the types of disturbances, an essential feature of the large disturbance is the change in the terminal voltage of VSG. Therefore, the large-disturbance stability issue of VSG can be modeled as how to respond properly to the disturbance of the terminal voltage.

III. Analysis of Electromagnetic Transient Process

A. *Electromagnetic Transient Performance Comparison of Different Virtual Impedance Control Structures*

As mentioned above, large disturbances would impact greatly on the terminal voltage of VSG and cause quite high electromagnetic transient currents in a very short time scale. For the suppression of the transient currents in such a short time, adding virtual impedance is a superior method [37].

Practically, the commonly used virtual impedance control structures mainly include the current-feedback-channel-type virtual synchronous steady-state impedance (CFC-VSSI) [38], the voltage-forward-channel-type VSSI (VFC-VSSI) [39], and the VFC virtual complete dynamic impedance (VFC-VCDI) [40], which are depicted, respectively, in Fig. 3. All the methods consist of two components, viz., virtual resistance and virtual inductance [8], [41]. The difference between CFC type and VFC type is that the former is to obtain voltage difference by multiplying the feedback current and the virtual impedance, whereas the latter is to obtain the current by dividing the voltage difference by

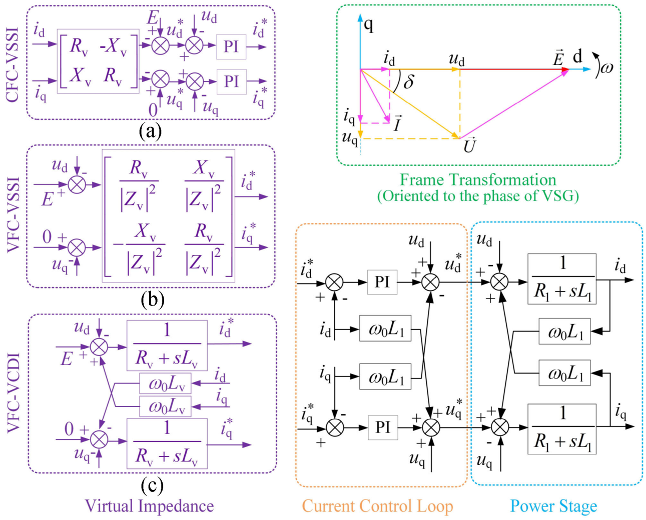

Fig. 3. Equivalent control block diagram of power stage and inner loop controller with different virtual impedance control structures. (a) Current-feedback-channel-type virtual synchronous steady-state impedance (CFC-VSSI). (b) Voltage-forward-channel-type virtual synchronous steady-state impedance (VFC-VSSI). (c) Voltage-forward-channel-type virtual complete dynamic impedance (VFC-VCDI).

the virtual impedance. The difference between VSSI and VCDI is that, the VSSI is to only mimic the impedance characteristics at the nominal frequency and ignore the differential items in the dynamic equations, whereas the VCDI is to copy the impedance characteristics completely in the whole frequency region.

The dynamic characteristics of different virtual impedance control structures will have crucial influences on the response of output currents; therefore, it is necessary to investigate which control structure is more advantageous to the optimization of the electromagnetic transient response.

According to the control block diagrams shown in Fig. 3, the equivalent output impedances under different virtual impedance control structures can be derived as given in the following procedure.

Taking the VFC-VSSI structure as shown in Fig. 3(b) for example, the synchronous virtual admittance matrix can be expressed as

$$\mathbf{Y}_{vdq,\text{VFC}-\text{VSSI}} = \begin{bmatrix} Y_{vdd,\text{VFC}-\text{VSSI}} & Y_{vdq,\text{VFC}-\text{VSSI}} \\ Y_{vqd,\text{VFC}-\text{VSSI}} & Y_{vqq,\text{VFC}-\text{VSSI}} \end{bmatrix} = \frac{1}{R_v^2 + X_v^2}\begin{bmatrix} R_v & X_v \\ -X_v & R_v \end{bmatrix} \quad (4)$$

where $\mathbf{Y}_{vdq}$ denotes the virtual synchronous admittance matrix in the *d*-*q* reference frame, the subscript "VFC-VSSI" is used to distinguish it from the other virtual impedance control structures, R_v and X_v are the set virtual resistance and synchronous virtual reactance, $X_v = \omega_0 L_v$, ω_0 is the nominal angular frequency, and L_v is the set virtual inductance.

Then, the current reference can be calculated by

$$\begin{bmatrix} i^*_{d,\text{VFC}-\text{VSSI}} \\ i^*_{q,\text{VFC}-\text{VSSI}} \end{bmatrix} = \begin{bmatrix} Y_{vdd,\text{VFC}-\text{VSSI}} & Y_{vdq,\text{VFC}-\text{VSSI}} \\ Y_{vqd,\text{VFC}-\text{VSSI}} & Y_{vqq,\text{VFC}-\text{VSSI}} \end{bmatrix} \times \begin{bmatrix} E - u_d \\ -u_q \end{bmatrix}. \quad (5)$$

The current control loop and power stage can be expressed together, that is

$$\begin{bmatrix} i_{d,\text{VFC}-\text{VSSI}} \\ i_{q,\text{VFC}-\text{VSSI}} \end{bmatrix} = \left(k_{\text{cp}} + \frac{k_{\text{ci}}}{s}\right)\frac{1}{R_1 + sL_1} \times \begin{bmatrix} i^*_{d,\text{VFC}-\text{VSSI}} - i_{d,\text{VFC}-\text{VSSI}} \\ i^*_{q,\text{VFC}-\text{VSSI}} - i_{q,\text{VFC}-\text{VSSI}} \end{bmatrix} \quad (6)$$

where k_{cp} and k_{ci} are the proportional and integral coefficients of PI controller of the current loop, respectively, R_1 and L_1 are the equivalent resistance and inductance of the output filter, respectively, and *s* is the Laplace operator.

The equivalent output admittance in the *d*-*q* reference frame can be defined as the ratio between the output current and the output voltage, namely

$$\begin{bmatrix} i_{d,\text{VFC}-\text{VSSI}} \\ i_{q,\text{VFC}-\text{VSSI}} \end{bmatrix} = \mathbf{Y}_{dq,\text{VFC}-\text{VSSI}}\begin{bmatrix} u_d \\ u_q \end{bmatrix} = \begin{bmatrix} Y_{dd,\text{VFC}-\text{VSSI}} & Y_{dq,\text{VFC}-\text{VSSI}} \\ Y_{qd,\text{VFC}-\text{VSSI}} & Y_{qq,\text{VFC}-\text{VSSI}} \end{bmatrix}\begin{bmatrix} u_d \\ u_q \end{bmatrix} \quad (7)$$

where $\mathbf{Y}_{dq}$ denotes the equivalent output admittance matrix.

Hence, according to (4)–(6), the output admittance of the VFC-VSSI can be derived as

$$\begin{cases} Y_{dd,\text{VFC}-\text{VSSI}}(s) = \frac{R_v(k_{\text{cp}}s + k_{\text{ci}})}{(R_v^2+X_v^2)[L_1 s^2 + (k_{\text{cp}}+R_1)s + k_{\text{ci}}]} \\ Y_{qd,\text{VFC}-\text{VSSI}}(s) = \frac{X_v(k_{\text{cp}}s + k_{\text{ci}})}{(R_v^2+X_v^2)[L_1 s^2 + (k_{\text{cp}}+R_1)s + k_{\text{ci}}]}. \end{cases} \quad (8)$$

It should be emphasized that although the power control loop also has an impact on the output impedance of the VSG through the phase perturbance caused by the power control, the specific impact of the power loop is reflected in two different ways: swing-rotating frame and steady-rotating frame [42], [43]. The former frame is aligned to the converter's *d*-*q* axes, while the latter rotates with a constant angular frequency. Regarding the studied VSG system in this article, the whole system is oriented to the output phase of the active power loop, i.e., the *d*-axis is aligned to the phasor of the inner potential *E* of the VSG as illustrated in Fig. 3, which is affiliated with the swing-rotating frame. According to the conclusions drawn by [42], the effect of the power loop can be equivalent to an additional impedance in series with (8) in the impedance circuit model, and the power loop only introduces a very small perturbance to output impedance and can be ignored in the swing-rotating frame. Hence, the output admittance characteristics of the studied VSG system in this article can be modeled by using (8), (37), and (39) well and truly. Moreover, due to the reasonable ignorance of the dynamics caused by the power loop, the output admittance expressions are always linear and thereby appropriate for different operating points. Therefore, they are also suitable for

TABLE I
MAIN PARAMETERS OF GRID-CONNECTED VSG SYSTEM

Symbol	Description	Value
P_n	Base active power	10 kW
U_n	Base voltage (phase-ground, RMS)	220 V
U_g	Grid voltage	220 V
U_{dc}	DC-side voltage of inverter	700 V
f_n	Nominal frequency	50 Hz
ω_0, ω_{ref}	Nominal angular frequency	100π rad/s
f_s	Switching frequency of inverter	10 kHz
E, E_{ref}	Virtual internal potential	222.3 V
X_L	Line inductance	8 mH
L_l	Filter inductance	3 mH
R_l	Filter resistance	0 Ω
X_s	Virtual reactance in steady state	0.3 p.u.
R_s	Virtual resistance in steady state	0.1 p.u.
P_{ref}	Active power reference	10 kW
J	Moment of inertia	1 kg·m^2
D	Equivalent damping coefficient	45 or 15 p.u.
k_{cp}	Proportional coefficient of current controller	3.5
k_{ci}	Integral coefficient of current controller	0
k_{vp}	Proportional coefficient of voltage controller	1.2665×10^{-3}
k_{vi}	Integral coefficient of voltage controller	372.5
I_{max}	Maximum tolerable current (peak value)	51A

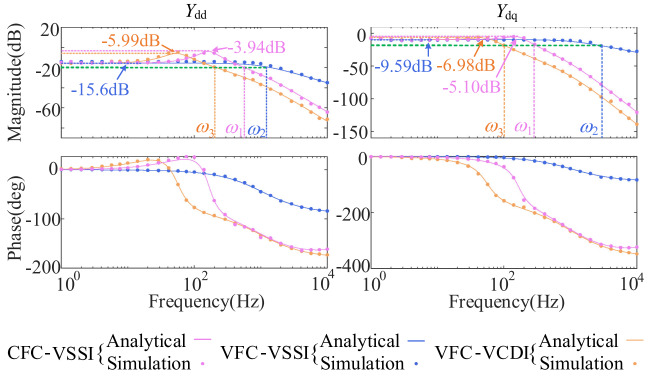

Fig. 4. Bode diagrams of output admittances of VSGs with different virtual impedance control structures.

the later large-disturbance analysis. Then, the equivalent output impedances under the other two virtual impedance control structures can also be derived similarly and the detailed derivation process is given in Appendix A.

To facilitate a comparative analysis of the effects of the different virtual impedance control structures, identical control parameters and electrical parameters, as listed in Table I, are set for the three control structures. Meanwhile, the proper values of the virtual impedance for different structures are set to obtain the same equivalent output admittance at the rated frequency. Then, the bode diagrams of Y_{dd} and Y_{dq} can be drawn in Fig. 4. Therein, the solid lines are the analytical results of the theoretical modeling and the dots are the frequency scanning results of the simulation model built in MATLAB. The simulation results coincide very closely with the theoretical results, which verifies the accuracy of the theoretical modeling. ω_1, ω_2, and ω_3 are the bandwidths of output admittances of VFC-VCDI, VFC-VSSI, and CFC-VSSI structures, respectively. It can be seen that the VFC-VSSI structure has the lowest resonance peak and the widest bandwidth, which implies its dynamic response has the smallest overshoot and needs the least settling time. Therefore, the VFC-VSSI structure has the most excellent performance during an electromagnetic transient response. Accordingly, the VFC-VSSI structure will be employed and analyzed further in this article.

B. *Output Impedance Boundary for Current Limiting During the Electromagnetic Transient Process*

According to (8), the output impedance at the nominal frequency is equal to the preset virtual impedance. It implies that the output impedance can be reshaped easily by regulating the virtual impedance. Considering the bandwidth of virtual impedance control are large adequately, as illustrated in Fig. 4, its dynamic process can be neglected. Thereby, the output current of the VFC-VSSI-based VSG can be expressed as

$$\begin{aligned}\begin{bmatrix} i_d \\ i_q \end{bmatrix} &= \frac{1}{|Z_v|^2}\begin{bmatrix} R_v & X_v \\ -X_v & R_v \end{bmatrix}\cdot\begin{bmatrix} E-u_d \\ -u_q \end{bmatrix} \\ &= \frac{1}{|Z_v|}\begin{bmatrix} \sin\varphi & \cos\varphi \\ -\cos\varphi & \sin\varphi \end{bmatrix}\cdot\begin{bmatrix} E-u_d \\ -u_q \end{bmatrix}\end{aligned} \tag{9}$$

where φ is the impedance angle, satisfying $\varphi = \arctan(R_v/X_v)$, $|Z_v|$ is the modulus of the impedance, viz. $|Z_v| = \sqrt{R_v^2 + X_v^2}$.

When the terminal voltage drops to U_{sag}, the output currents in *d*- and *q*-axis are written as

$$\begin{cases} i_d = \frac{1}{|Z_v|}\left[E\sin\varphi + U_{\text{sag}}\sin(\delta-\varphi)\right] \\ i_q = \frac{1}{|Z_v|}\left[-E\cos\varphi + U_{\text{sag}}\cos(\delta-\varphi)\right] \end{cases} \tag{10}$$

where U_{sag} is the terminal voltage after the large disturbance and δ is the power angle, namely the phase difference between the virtual inner potential and terminal voltage. According to Park inverse transformation, the α-axis current in the α-β reference frame yields

$$i_\alpha = i_d\sin(\omega t) + i_q\cos(\omega t). \tag{11}$$

Therefore, the maximum value of the current can be obtained by calculating the extremum of (11), namely

$$i_{\alpha\max} = -\frac{E}{|Z_v|}\cos(\omega t_{\max} + \varphi) + \frac{U_{\text{sag}}}{|Z_v|}\cos(\omega t_{\max} - \delta + \varphi) \tag{12}$$

where δ_0 can be calculated by (17) given later and $t_{\max}$ is the time that the maximum current appears, which is given by

$$t_{\max} = \frac{1}{\omega}\left\{\pi + \arctan\left[\frac{E\sin\varphi + U_{\text{sag}}\sin(\delta-\varphi)}{-E\cos\varphi + U_{\text{sag}}\cos(\delta-\varphi)}\right]\right\}. \tag{13}$$

It can be seen from (12) that the modulus of the output impedance plays a crucial role in the maximum current value $i_{\alpha\max}$, whereas the corresponding occurrence time $t_{\max}$ is mainly determined by the impedance ratio. Supposing the maximum tolerable steady-state current is $I_{\max}$, thereby the maximum current must satisfy

$$i_{\alpha\max} \leq I_{\max} \tag{14}$$

where $I_{\max}$ is the maximum tolerable current.

Accordingly, by substituting (12) into (14), the output impedance boundary for current limiting can be obtained as

$$|Z_v| \geq -\frac{E}{I_{\max}} \cos\left(\omega t_{\max} + \varphi\right) + \frac{U_{\text{sag}}}{I_{\max}} \cos\left(\omega t_{\max} - \delta + \varphi\right). \tag{15}$$

Obviously, (15) implies that the magnitude boundary of the virtual impedance is the function of virtual impedance angle φ, which equals $\arctan(R_v/X_v)$. Therefore, the magnitude boundary of the virtual impedance expressed by (15) can be illustrated by a two-dimensional (2-D) curve in a rectangular coordinate system, where the x-axis is the impedance ratio R_v/X_v, and the y-axis is the virtual impedance magnitude $|Z_v|$.

IV. Analysis of Electromechanical Transient Process

As it is explained in Section II, the essence of the large-disturbance problem of grid-connected VSG systems is how to properly react to the change of the terminal voltage of VSG. Accordingly, this section will take the three-phase voltage sag fault, a type of common and severe large disturbance, as an example to analyze the electromechanical transient stability issue.

When the grid voltage sag causes the terminal voltage of VSG to drop, the output active power of VSG will also decrease. Consequently, the power imbalance between the active power reference and the output active power will accelerate the output frequency of the VSG and then increase the power angle. As a result, the power angle would probably exceed the maximum permissible stable angle and become unstable. This is the electromechanical transient stability or transient power angle stability problem of VSG that will be discussed in this section.

The output impedance plays a prominent part in the electromechanical transient process after a large disturbance because it can impact the power angle characteristics of VSG. Hence, the electromechanical transient stability can be enhanced by tuning the output impedance. However, when the electromagnetic and electromechanical transient stability during a large disturbance process are considered together, the design of the output impedance is frequently a contradictory problem. For example, when a voltage sag occurs, the virtual impedance should be enlarged to suppress the transient current; yet for the transient power angle stability issue, the larger output impedance will lower the power angle curve further and it is prone to make the VSG system more difficult to stabilize. Unfortunately, although the design of output impedance has been a matter of great concern in previous articles, such a large-disturbance stability issue is still seldomly addressed.

To facilitate the analysis, the large disturbances are divided into two types according to whether there is an equilibrium point after the large disturbance. The power angle curve can be drawn in Fig. 5 and it is expressed mathematically as [44]

$$P = \frac{3EU}{|Z|} \sin\left(\delta + \varphi\right) - \frac{3U^2 \sin\varphi}{|Z|}. \tag{16}$$

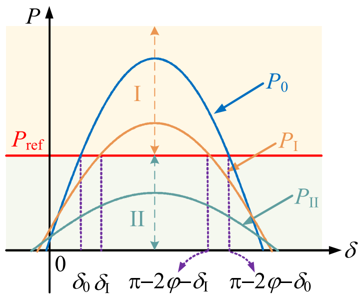

Fig. 5. Power angle curves and classification of large disturbances (Type-I: the peak of postdisturbance power curve is located in region I; Type-II: the peak of postdisturbance power curve is located in region II).

When a large disturbance appears, the power angle curve will be modified correspondingly. If the peak of the postdisturbance power angle curve is located in the region I, where the power reference P_{ref} still intersects with the power angle curve, that means there is still a theoretical equilibrium point where the system can stay steadily, namely δ_I. This type of large disturbance is named Type-I large disturbance for convenience in this article. When a Type-I large disturbance occurs, the system can still reach a new acceptable steady-state operating point. Commonly, a load/generator switching or a small voltage sag belongs to this type. If the peak of the postdisturbance power curve is located in region II, there will be no equilibrium points after the disturbance. This type of large disturbance is called Type-II large disturbance for differentiation from the first type, which is so serious that the system can keep running for only a short time and cannot reach a new steady state unless proper measures are taken in time to help the system ride through the large disturbance stably. Generally, a severe voltage sag, e.g., three-phase to ground short circuit, belongs to this type of event.

A. *Type-I Large Disturbance: Equilibrium Points Still Exist After the Large Disturbance Occurs*

When the terminal voltage of VSG drops following a grid voltage sag fault, the power angle curve of VSG shifts from P_0 to P_I, as shown in Fig. 5. Before the voltage sag, the equilibrium points of the system are (δ_0, $\Delta\omega = 0$) and ($\pi-2\varphi-\delta_0$, $\Delta\omega = 0$). It should be emphasized that $\Delta\omega$ means the deviation from the grid angular frequency here, instead of a small disturbance of ω. After the voltage sag, the system still has two new equilibrium points (δ_I, $\Delta\omega = 0$) and ($\pi-2\varphi-\delta_{\text{I}}$, $\Delta\omega = 0$). Therein, the equilibrium points on the left of the peaks of the power angle curves are the stable equilibrium points, while the right equilibrium points are the maximum critical points. Once the system exceeds the right maximum critical points, the system would never come back to the stable points again and become unstable finally.

Based on (16), the power angle δ at the stable equilibrium point can be obtained as

$$\delta = \arcsin\left(\frac{P_{\text{ref}} + \frac{3U^2 \sin\varphi}{|Z|}}{\frac{3EU}{|Z|}}\right) - \varphi. \tag{17}$$

To ensure the existence of the equilibrium points, the power angle δ at the stable equilibrium point must satisfy

$$\arcsin\left(\frac{U}{E}\sin\varphi\right)-\varphi<\delta<\frac{\pi}{2}-\varphi. \tag{18}$$

Combining (17) with (18) and substituting the corresponding variables after the voltage sag occurs, the impedance boundaries for the existence of the equilibrium points during the disturbance can be derived as

$$0<|Z|<\frac{3}{P_{\mathrm{ref}}}U_{\mathrm{sag}}\left(E-U_{\mathrm{sag}}\sin\varphi\right) \tag{19}$$

where U_{sag} is the terminal voltage after the large disturbance occurs.

To tackle the nonlinear process caused by the large disturbance, the Lyapunov energy function method is employed here as the stability criterion to discuss the electromechanical transient stability issue. According to Lyapunov's stability theory, there is the following theorem [16].

For a dynamic system described by $\dot{\mathbf{x}}=\mathbf{F}(\mathbf{x})$, if a positive definite scalar function $V(\mathbf{x})$around its equilibrium point $\hat{\mathbf{x}}$ satisfies $\dot{V}(\mathbf{x})<0$, then for any initial conditions $\mathbf{x}_0$, the system is asymptotically stable at the equilibrium point when it satisfies

$$V\left(\mathbf{x}_0\right)<V_{\mathrm{cr}} \tag{20}$$

where $\mathbf{x}$ is the state vector of the dynamic system and $V_{\mathrm{cr}}(\tilde{\mathbf{x}}\neq\hat{\mathbf{x}})$ is the value of Lyapunov function at the nearest equilibrium point.

Based on this theorem, (20) can be used as the stability criterion to analyze the output impedance boundaries. It should be emphasized that, although (20) is merely a sufficient condition of stability, not the necessary condition, a Lyapunov function with a clear physical meaning can still give a proper stability assessment that very closely coincides with the real stability region, and this article will choose such a function. Meanwhile, the stability margin should generally be set apart. For these reasons, it is rational to use (20) as the mathematical method to find the impedance boundaries in this article. The accuracy will also be verified by the latter experimental results.

According to (3) and (16), the swing of the power angle after the voltage sag occurs without considering the damping effect can be described by

$$M\frac{\mathrm{d}(\omega-\omega_g)}{\mathrm{d}t}=P_{\mathrm{ref}}-\left(\frac{3EU_{\mathrm{sag}}}{|Z|}\sin\left(\delta+\varphi\right)-\frac{3U_{\mathrm{sag}}^2\sin\varphi}{|Z|}\right). \tag{21}$$

Integrating (21) from the equilibrium point after the voltage sag appears, viz., (δ_I, $\Delta\omega=0$) gives

$$\begin{aligned}V&=\underbrace{\int_0^{\Delta\omega}\left(M\Delta\omega\right)\mathrm{d}\Delta\omega}_{E_{\mathrm{k}}}\\&\quad\underbrace{-\int_{\delta_{\mathrm{I}}}^{\delta}\left\{P_{\mathrm{ref}}-\left[\frac{3EU_{\mathrm{sag}}}{|Z|}\sin\left(\delta+\varphi\right)-\frac{3U_{\mathrm{sag}}^2\sin\varphi}{|Z|}\right]\right\}\mathrm{d}\delta}_{E_{\mathrm{p}}}\\&=\frac{1}{2}M\Delta\omega^2-\left(P_{\mathrm{ref}}+\frac{3U_{\mathrm{sag}}^2\sin\varphi}{|Z|}\right)\left(\delta-\delta_{\mathrm{I}}\right)\\&\quad-\left(\frac{3EU_{\mathrm{sag}}}{|Z|}\left[\cos\left(\delta+\varphi\right)-\cos\left(\delta_{\mathrm{I}}+\varphi\right)\right]\right).\end{aligned} \tag{22}$$

It can be observed that (22) is a function with a clear physical meaning and describes exactly the conversion between kinetic energy E_k and potential energy E_p in the power swing process and therefore is used as Lyapunov energy function in the latter analysis. The demonstration of how (22) satisfies the Lyapunov function conditions is given in Appendix B.

In the case of Type-I large disturbance, by substituting the initial point (δ_0, $\Delta\omega_0=0$) into (22), the initial energy $V(\delta_0, 0)$ can be obtained as

$$\begin{aligned}V\left(\delta_0,0\right)=&-\left(P_{\mathrm{ref}}+\frac{3U_{\mathrm{sag}}^2\sin\varphi}{|Z|}\right)\left(\delta_0-\delta_{\mathrm{I}}\right)\\&-\left(\frac{3EU_{\mathrm{sag}}}{|Z|}\left[\cos\left(\delta_0+\varphi\right)-\cos\left(\delta_{\mathrm{I}}+\varphi\right)\right]\right).\end{aligned} \tag{23}$$

The maximum critical point is ($\pi-2\varphi-\delta_I$, $\Delta\omega=0$). Therefore, similarly, the critical energy V_{cr} can be derived as

$$\begin{aligned}V_{\mathrm{cr}}&=V\left(\pi-2\varphi-\delta_I,0\right)\\&=-\left(P_{\mathrm{ref}}+\frac{3U_{\mathrm{sag}}^2\sin\varphi}{|Z|}\right)\left(\pi-2\varphi-2\delta_I\right)\\&\quad+\frac{6EU_{\mathrm{sag}}}{|Z|}\cos\left(\delta_I+\varphi\right).\end{aligned} \tag{24}$$

According to Lyapunov's stability criterion described by (20), the impedance boundary for the transient power angle stability can be given by

$$\begin{aligned}&\left(P_{\mathrm{ref}}\,|Z|+3U_{\mathrm{sag}}^2\sin\varphi\right)\left(-\pi+2\varphi+\delta_0+\delta_{\mathrm{I}}\right)\\&\quad+3EU_{\mathrm{sag}}\left[\cos\left(\delta_{\mathrm{I}}+\varphi\right)+\cos\left(\delta_0+\varphi\right)\right]>0\end{aligned} \tag{25}$$

where δ_0 and δ_I can be calculated by using (17).

Moreover, the output impedance should also be able to ensure stable operation after the fault is cleared. Namely, when the terminal voltage returns to the normal level, the equilibrium points should still exist. Similar to (19), the impedance boundary for the existence of the equilibrium points after the disturbance can be obtained as

$$0<|Z|<\frac{3}{P_{\mathrm{ref}}}U_0\left(E-U_0\sin\varphi\right) \tag{26}$$

where U_0 is the normal terminal voltage.

As has been mentioned before, the boundaries described by (15), (19), (25), and (26) can be illustrated by 2-D curves in the rectangular coordinate system with *R*/*X* and |*Z*| as the *x*-axis and *y*-axis, respectively. Accordingly, these boundaries encircle a stable region in the rectangular coordinate system, which is the desired range of the output impedance of VSG when a Type-I large disturbance occurs. For example, when U_{sag} equals 0.6 p.u. and $I_{\max}$ equals 51 A, the boundaries and the encircled stable region can be drawn in Fig. 6.

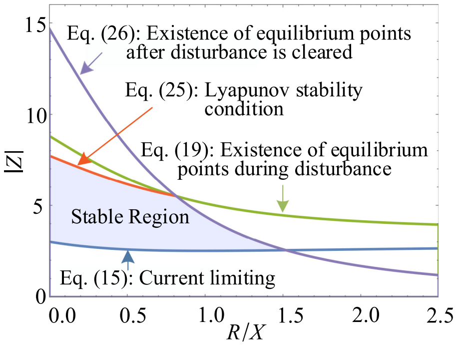

Fig. 6. Output impedance boundaries and encircled stable region for a Type-I large disturbance (taking 0.4 p.u. terminal voltage sag for an example here).

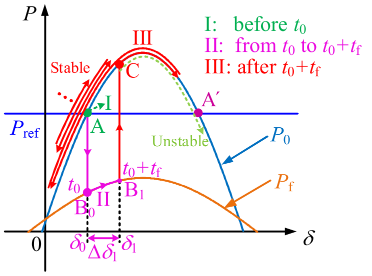

Fig. 7. Physical stages of Type-II large disturbance (Stage I: before t_0, at A; Stage II: from t_0 to $t_0 + t_f$, magenta accelerating trajectory along the curve of P_f, A→B_0→B_1; Stage III: after $t_0 + t_f$, red oscillating trajectory along P_0, B_1→C→· · ·→A/unstable).

According to Fig. 6, once the impedance ratio R/X is determined, the range of the desired magnitude of output impedance will be obtained. Generally, the upper boundaries are related to the electromechanical transient stability, while the lower boundary is to limit electromagnetic transient current. To retain a larger stability margin, it is preferable to select the virtual impedance magnitude that is slightly larger than the lower boundary and much smaller than the upper boundary. Besides, a proper resistance component is also recommended for taking the advantage of its damping effect on the transient process.

B. Type-II Large Disturbance: Equilibrium Points Do Not Exist After the Large Disturbance Occurs

For Type-II large disturbance, $P_{\rm ref}$ is always greater than the actual output active power during the disturbance, such as the postdisturbance power angle curve $P_{\rm II}$ shown in Fig. 5. In this case, the output frequency of the VSG will stay in the state of continuous acceleration, thereby leading to a sustained increase of the power angle. Eventually, the power angle will jump over the maximum critical point and become unstable. Under this circumstance, the VSG system must take measures promptly to maintain stability.

On account of the contradiction between the electromagnetic transient stability and electromechanical transient stability, namely the former requires a larger impedance while the latter expects a smaller one, there is not a fixed virtual impedance value suitable for the whole transient process of Type-II large disturbance anymore. To resolve this contradiction, the whole transient process will be divided into several physical stages in chronological order to analyze, respectively. Then, the desired virtual impedances for different stages can be determined.

The whole physical process of Type-II large disturbance can be illustrated in Fig. 7. Assuming the disturbance occurs at t_0, the power angle curve shifts from P_0 to P_f. As a result, the input power and output power become imbalanced, and then the frequency and power angle begin to accelerate. Until t_0+t_f, the fault is cleared and the power angle curve returns to P_0. If the VSG system can continue operating stably, it will swing along the curve of P_0 back and forth until the steady state is reached. If cannot, the power angle will jump over A′ during the swing along P_0, thereby becoming unstable.

Accordingly, the whole transient process is divided into three physical stages as listed in Table II. Stage I is before the occurrence of the disturbance, in which the system is located at A stably. Stage II is from the occurrence of disturbance to the moment of the clearance of disturbance, whose motion trajectory is marked with magenta color in Fig. 7. Stage III describes the dynamic oscillation after clearing the disturbance, as marked by the red color.

For different stages, the VSG should handle different problems, therefore having respective desired values of the virtual impedance. The following will give a detailed analysis of the three stages.

To begin with, for ease of understanding the later contents, the state variables are declared here beforehand, viz., the power angle δ, the angular frequency deviation from the grid angular frequency $\Delta\omega$, and the angular acceleration ε. It should be noted that "Δ" denotes a deviation in this article, instead of a small disturbance. Accordingly, the corresponding state variables at A, B_0, and B_1 can be listed in Table III, respectively.

1) Stage I: Before the Type-II large disturbance occurs, the VSG operates normally at A with the normal virtual impedance Z_s. The state variables in this stage determine the initial conditions of the next stage, and therefore should be calculated for the analysis of Stage II. At point A, the swing equation of the VSG can be described by

$$M\frac{\mathrm{d}\Delta\omega}{\mathrm{d}t} = P_{\rm ref} - \left[\frac{3EU}{|Z_{\rm s}|}\sin\left(\delta+\varphi_{\rm s}\right) - \frac{3U^2\sin\varphi_{\rm s}}{|Z_{\rm s}|}\right] - D\Delta\omega \tag{27}$$

where $|Z_s|$ and φ_s are the magnitude and impedance angle of the virtual impedance used for the normal case, respectively.

According to (17), the expression of power angle δ_0 at the equilibrium point A ($\delta_A = \delta_0$, $\Delta\omega_A = 0$, and $\varepsilon_A = 0$) can be written as

$$\delta_0 = \arcsin\left(\frac{P_{\rm ref} + \frac{3U^2\sin\varphi_s}{|Z_s|}}{\frac{3EU}{|Z_s|}}\right) - \varphi_s \tag{28}$$

where $\arcsin(\frac{U}{E}\sin\varphi_s) - \varphi_s < \delta_0 < \frac{\pi}{2} - \varphi_{\rm s}$.

2) Stage II: During Stage II, the severe drop of the terminal voltage will cause a huge electromagnetic transient current. Therefore, the top concern in this stage is to limit the overcurrent. According to (15), the impedance boundary for limiting the

TABLE II
THREE STAGES OF TYPE-II DISTURBANCE

Stage	Time	Trajectory in Fig. 7	Symbol of Z	Descriptions
I	Before t_0	A	Z_s	Before the occurrence of the disturbance
II	From t_0 to t_0+t_f	A→B$_0$→B$_1$	Z_f	From the occurrence of disturbance to the moment of the disappearance of disturbance
III	After t_0+t_f	B$_1$→C→A/unstable	Z_r	From the moment of the disturbance clearing to the moment of reaching a new steady state

TABLE III
STATE VARIABLES DURING STAGE II

Time	Locations	State variables
Before t_0	A	$(\delta_A = \delta_0, \Delta\omega_A = 0, \varepsilon_A = 0)$
At t_0	B$_0$	$(\delta_0, \Delta\omega_0 = 0, \varepsilon_0)$
At t_0+t_f	B$_1$	$(\delta_1, \Delta\omega_1, \varepsilon_1)$

TABLE IV
SYMBOLS AND DESIGN RULES OF VIRTUAL IMPEDANCE FOR DIFFERENT CASES

Cases		Symbols	Design criteria
Normal operation		Z_s, φ_s	Traditional methods
Type I		Z_p, φ_p	(15), (19), (25) and (26)
Type II	Stage I	Z_s, φ_s	Traditional methods
	Stage II	Z_f, φ_f	(29)
	Stage III	Z_r, φ_r	(32)

electromagnetic transient current is obtained as

$$|Z_f| \geq -\frac{E}{I_{\max}}\cos\left(\omega t_{\max}+\varphi_f\right) + \frac{U_{\text{sag}}}{I_{\max}}\cos\left(\omega t_{\max}-\delta_0+\varphi_f\right) \qquad (29)$$

where $|Z_f|$ and φ_f are the magnitude and impedance angle of the virtual impedance specifically used for Stage II, respectively; $t_{\max}$ can be calculated by (13) where the variables should employ the values during Stage II.

Furthermore, the state variables of Stage II at point B_1, i.e., the power angle δ_1 and the angular frequency deviation $\Delta\omega_1$, are measured by using a phase lock loop (PLL) for the assessment of the electromechanical stability during Stage III. Because δ_1 and $\Delta\omega_1$ are the initial conditions of the dynamic process of Stage III, they play an important role in the power angle stability. Moreover, it should be emphasized that the PLL is only used for the calculation of the next output impedance at the moment to turn into Stage III, so it has no impact on the synchronization characteristics of the VSG.

3) Stage III: After the large disturbance disappears, the terminal voltage will recover. Assuming the restored terminal voltage is U_{post}, the power angle swing equation becomes

$$M\frac{\mathrm{d}\Delta\omega}{\mathrm{d}t} = P_{\text{ref}} - \left[\frac{3EU_{\text{post}}}{|Z_r|}\sin\left(\delta+\varphi_{\text{r}}\right) - \frac{3U_{\text{post}}^2\sin\varphi_r}{|Z_r|}\right] - D\Delta\omega \qquad (30)$$

where $|Z_r|$ and φ_r are the magnitude and impedance angle of the virtual impedance specifically used for Stage III, respectively.

To assess whether the system can achieve asymptotic stability again, similar to the foregoing analysis of the Type-I large disturbance, the Lyapunov stability theorem is also employed. As described before, the Lyapunov energy function is written as

$$V = \frac{1}{2}M\Delta\omega^2 - \left(P_{\text{ref}} + \frac{3U_{\text{post}}^2\sin\varphi_{\text{r}}}{|Z_r|}\right)\left(\delta-\delta_r\right) - \frac{3EU_{\text{post}}}{|Z_r|}\left[\cos\left(\delta+\varphi_r\right) - \cos\left(\delta_r+\varphi_r\right)\right] \qquad (31)$$

where δ_r is the stable equilibrium point after the voltage recovery and can be calculated by replacing the relevant variables in (28).

By substituting the maximum critical point of this stage, viz. $(\pi-2\varphi_r-\delta_r,\ \Delta\omega = 0)$, and the observed initial conditions, viz. $(\delta_1,\ \Delta\omega_1)$, into (31), the critical energy value V_{cr} and the initial energy value $V(\delta_1,\ \Delta\omega_1)$ can be obtained. Then, according to Lyapunov's stability criterion described by (20), the impedance boundary for the electromechanical stability can finally be obtained similar to the derivation of (25), that is

$$\left(P_{\text{ref}} + \frac{3U_{\text{post}}^2\sin\varphi_r}{|Z_r|}\right)\left(\delta_1+2\varphi_r+\delta_r-\pi\right) + \frac{3EU_{\text{post}}}{|Z_r|}\left[\cos\left(\delta_r+\varphi_r\right)+\cos\left(\delta_1+\varphi_r\right)\right] - \frac{1}{2}M\Delta\omega_1^2 > 0. \qquad (32)$$

V. LARGE-DISTURBANCE STABILITY ENHANCEMENT STRATEGY BY USING ADAPTIVE VIRTUAL IMPEDANCE

Based on the aforementioned theoretical analysis, a novel adaptive virtual impedance optimization control strategy to enhance both the electromagnetic and electromechanical large-disturbance stability of VSG is proposed in this section, whose control flow chart is depicted in Fig. 8. The symbols and design rules of the virtual impedance for different cases are briefly summarized in Table IV.

Although this article has given the analytic expressions of the design criteria, the lookup table approach is recommended in the practical implementation by a digital processor due to its simplicity and rapidity. The designer can make the tables in advance by referring to the theoretical stability criteria as given above. After that, the VSG system can automatically select the desired virtual impedance by looking up the premade tables when it encounters an unexpected large disturbance.

According to the types of large disturbances, as analyzed above, the control procedure is divided into two scenarios to be addressed, respectively. To distinguish the two scenarios, the

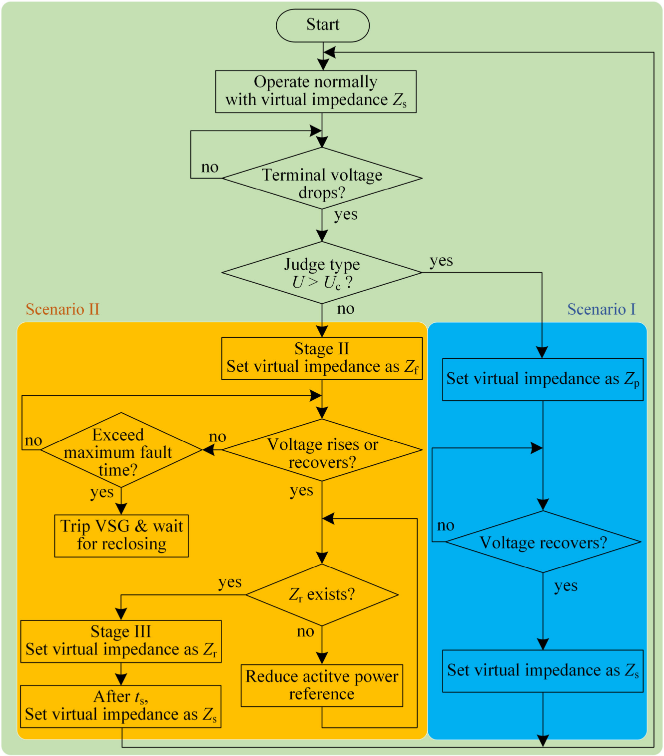

Fig. 8. Control flowchart of the proposed large-disturbance stability enhancement strategy with two different scenarios.

boundary of critical terminal voltage between them should be derived. As shown in Fig. 5, the boundary is located at the place where the power reference line is tangent to the power angle curve, namely

$$P_{\text{ref}} = \frac{3EU_{\text{c}}}{|Z_{\text{c}}|}\sin\left(\delta_c + \varphi_c\right) - \frac{3U_c^2 \sin\varphi_c}{|Z_c|} \tag{33}$$

where $\delta_c = \pi/2 - \varphi_c$. The subscript "$c$" symbolizes the critical values between the two scenarios. To leave some margin, $|Z_c|$ is defined as the minimum value of (15).

By solving (33), the critical voltage can be obtained as

$$U_c = \frac{3E - \sqrt{9E^2 - 12P_{\text{ref}}\,|Z_c|\sin\varphi_c}}{6\sin\varphi_c}. \tag{34}$$

The VSG monitors the terminal voltage in real time. When the terminal voltage is lower than 0.9 p.u., the VSG triggers the large-disturbance stability enhancement strategy and then judges the disturbance type by comparing the detected voltage with the critical voltage.

If $U > U_c$, representing that the disturbance belongs to the Type-I large disturbance (Scenario I), the virtual impedance during the large disturbance will be chosen from the pre-made lookup tables, which is symbolized by Z_p. In this case, the stability can be maintained throughout the whole large-disturbance transient process. Finally, when the system detects that the terminal voltage returns to the normal state, the impedance will be restored to the normal value before the large disturbance, viz., Z_s, by using a ramp control so that the system can exhibit optimal power transmission capability and power control performance.

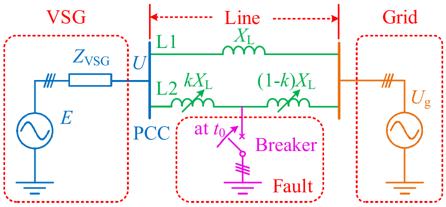

Fig. 9. Circuit structure of the grid-connected VSG tested system.

If the detection tells that it is the Type-II large disturbance (Scenario II), namely $U < U_c$, the virtual impedance should be chosen for different physical stages, as explained in Section IV-B. When the system detects the occurrence of a Type-II large disturbance, it immediately triggers a switch of virtual impedance from the normal value Z_s before disturbance (Stage I) to Z_f, which can be set by using the lower boundary (29) for current limiting at Stage II [and can also be set by looking up the tables designed beforehand according to (29)]. After that, the system waits for the rise or recovery of the terminal voltage, which indicates the clearing of the large disturbance. When the system detects the rise in terminal voltage, it should judge whether the system can return to the left equilibrium point stably or not at the moment of voltage rise, i.e., whether the desired impedance can be obtained by solving (32) and meanwhile this desired impedance can satisfy (15), where U_{sag} should be replaced with the postdisturbance voltage U_{post}.

If the system can approach the stable operating point asymptotically, the virtual impedance value is set to Z_r according to the impedance boundary (32) for Stage III. After t_s, the system returns to the steady state and restores the virtual impedance to the normal value Z_s by using a ramp control in order to make the system exhibit the optimal small-disturbance dynamic performance.

However, if the system cannot return to stability, it should further take some measures, e.g., reducing the active power reference [25], to help the converter ride through this stage. Repeat the above actions until the desired impedance that can make the system return to some steady-state point is found. Then, the procedure enters Stage III. Similarly, after t_s, the virtual impedance is restored to Z_s by using a ramp control.

Particularly, during Stage II, if the duration of the large disturbance exceeds the critical value specified by the power systems, the VSG is entitled to open the circuit breakers to trip itself. After that, the VSG awaits the fault clearing and then recloses to the system.

VI. EXPERIMENTAL RESULTS

In this section, experiments are conducted to verify the accuracy of impedance boundaries concluded from the theoretical analysis and the effectiveness of the proposed stability improvement method by using a hardware-in-loop platform. The circuit structure of the tested grid-connected VSG system is given in Fig. 9, and the main parameters are listed in Table I. The

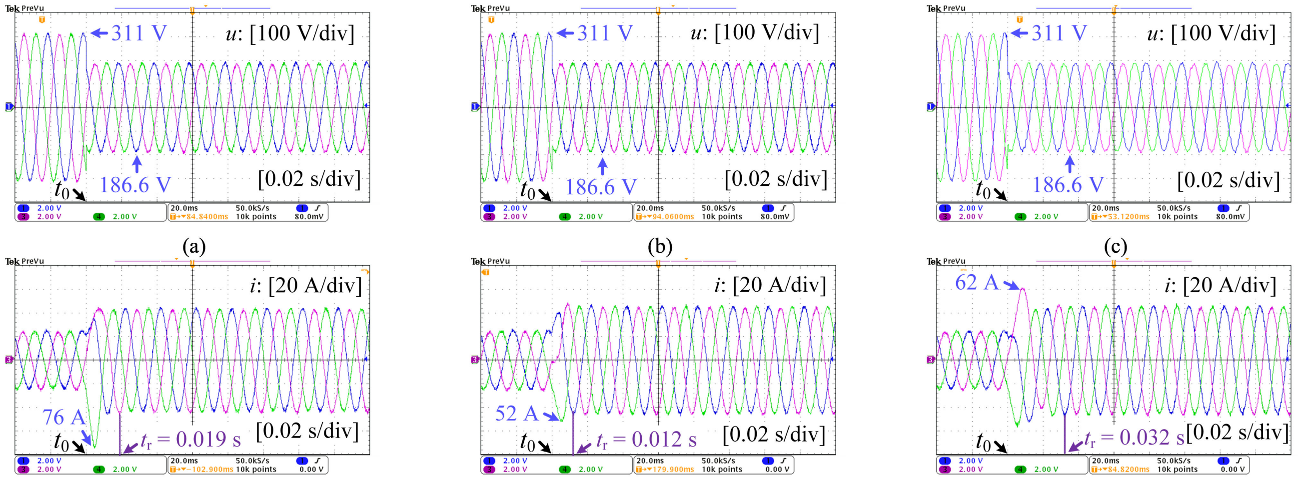

(a) (b) (c)

(d) (e) (f)

Fig. 10. Terminal voltage and output current waveforms after a 0.4 p.u. terminal voltage sag at t_0 under different virtual impedance control structures. Voltage: (a) CFC-VSSI, (b) VFC-VSSI, and (c) VFC-VCDI. Current: (d) CFC-VSSI, (e) VFC-VSSI, and (f) VFC-VCDI.

VSG system, equivalent to a controlled voltage source in series with an output impedance, is connected to the grid through a double-circuit transmission line. A breaker is controlled to be closed to simulate a short-circuit fault at $L2$. The k is selected properly to simulate different locations where the fault occurs, and thereby the VSG system will undergo different levels of voltage sag at the PCC. The line inductance is 8 mH.

A. Verification of the Dynamic Performance of Different Virtual Impedance Control Structures

First, the dynamic response performance of different virtual impedance control structures is compared by observing the electromagnetic transient currents after a short-circuit fault. All the three schemes employ the same virtual impedance at the nominal frequency, namely $R_v = 0.0693$ p.u. and $X_v = 0.1088$ p.u. before t_0, $R_v = 0.0836$ p.u. and $X_v = 0.1672$ p.u. after t_0. k in Fig. 9 is set to 0.9, and the breaker is closed at t_0. In this case, the terminal voltage at PCC will drop by 0.4 p.u. (viz., $U \approx 0.6$ p.u. $\approx$ 186 V in peak value). The terminal voltage and the output current waveforms of VSGs with different virtual impedance control structures are shown in Fig. 10.

It can be observed that the CFC-VSSI method exhibits the largest peak current (76 A), next is the VFC-VCDI (62 A), and the VFC-VSSI has the smallest one (52 A). With regard to the response speed, VFC-VSSI is the fastest (0.012 s), CFC-VSSI takes second place (0.019 s), and VFC-VCDI is the slowest (0.032 s). Therefore, VFC-VSSI shows the best dynamic performance in the aspect of overcurrent limitation. The above experimental results agree with the theoretical conclusions obtained from the bode diagrams shown in Fig. 4.

B. Verification of Impedance Boundary for Electromagnetic Transient Current Limiting

This section is to verify the correctness of the impedance boundary for the current limiting derived in Section III. The virtual impedance control employs the VFC-VSSI structure.

According to the impedance boundaries as shown in Fig. 6, where the maximum tolerable current is set to 51 A in peak value and the terminal voltage U_{sag} is set to 0.6 p.u., $R/X = 1$ and $|Z| = 2.51\ \Omega$ is located on the impedance boundary of the current limiting, while $R/X = 1$ and $|Z| = 2.1\ \Omega$ is beyond the safe operating area.

To verify this, the terminal voltage is designed to generate a 0.4 p.u. voltage sag at t_0 by letting k equal 0.9. The current waveforms of Case I ($R/X = 1$ and $|Z| = 2.51\ \Omega$) and Case II ($R/X = 1$ and $|Z| = 2.1\ \Omega$) are shown in Fig. 11(b) and (d), respectively, and the terminal voltage are shown in Fig. 11(a) and (c). Fig. 11(b) indicates that the peak value of the transient current is limited to about 51 A, which is consistent with the predesigned theoretical value. Fig. 11(d) shows that the peak value of the transient current is 60 A, which exceeds the maximum tolerable current. The experimental results validate the accuracy of the current limiting boundary calculated by (15).

C. Verification of Impedance Boundaries for Electromechanical Transient Power Angle Stability

This section is to prove the correctness of the impedance boundaries aiming at the electromechanical transient stability proposed in Section IV.

1) Type-I Large Disturbance: According to Fig. 6, the virtual impedances $R/X = 0.5$, $|Z| = 6.2\ \Omega$ (within the stable region) and $R/X = 0.5$, $|Z| = 6.5\ \Omega$ (outside the stable region) are set in the experiment, respectively. D equals 45 p.u. In this case, letting $k = 0.99$ can obtain a 0.4 p.u. sag of the terminal voltage when the breaker is closed at t_0. The experimental results are shown in Fig. 12.

It can be seen that, when $R/X = 0.5$ and $|Z| = 6.2\ \Omega$, VSG can continue operating stably after several convergent oscillations because of the proper choice of virtual impedance. Differently, when $R/X = 0.5$ and $|Z| = 6.5\ \Omega$, since the virtual impedance value is beyond the stable region, at about 3 s after the occurrence of the disturbance, the power waveforms begin

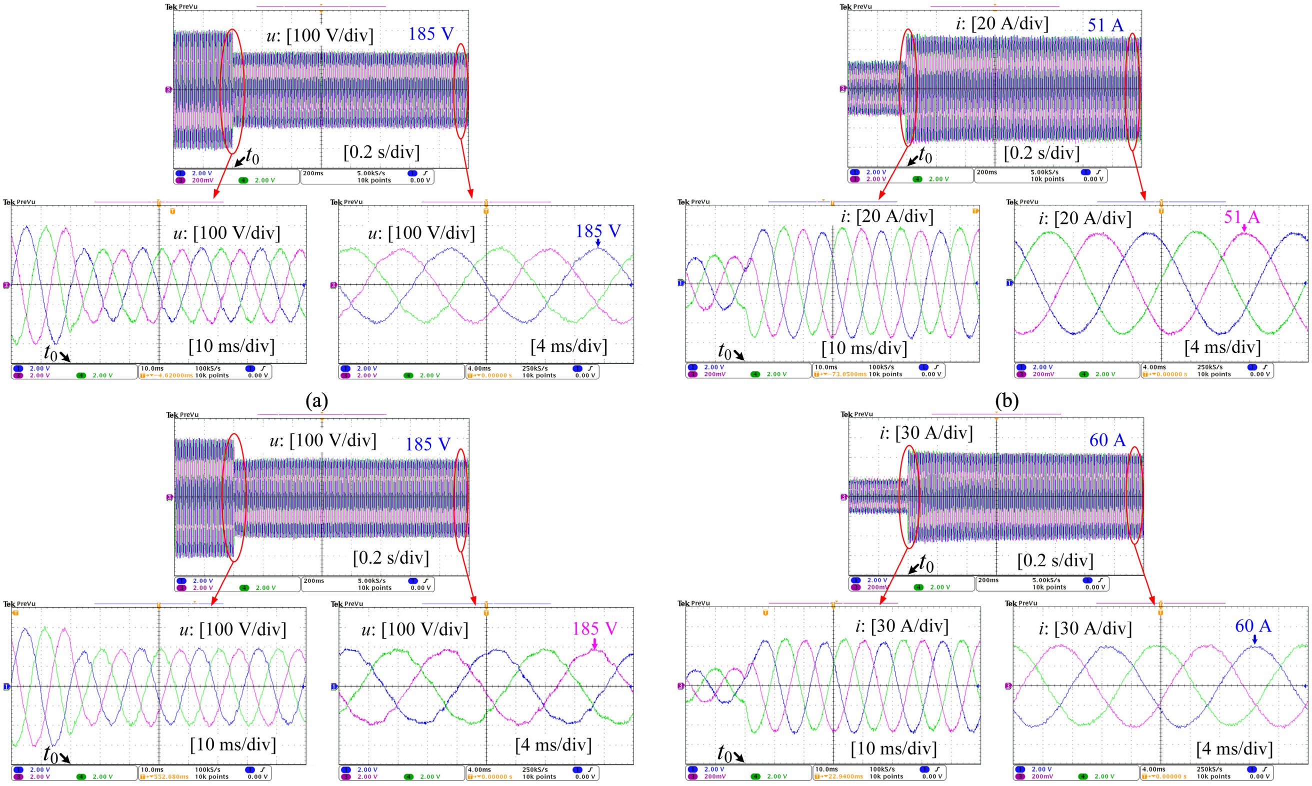

(a) (b)

(c) (d)

Fig. 11. Terminal voltage and electromagnetic transient current response waveforms after a 0.4 p.u. terminal voltage sag at t_0 with different virtual impedance values under VFC-VSSI control structure. (a) and (b): $R/X = 1$ and $|Z| = 2.51\ \Omega$. (c) and (d): $R/X = 1$ and $|Z| = 2.1\ \Omega$.

Case 1: $R/X = 0.5$, $|Z_r| = 6.2\ \Omega$

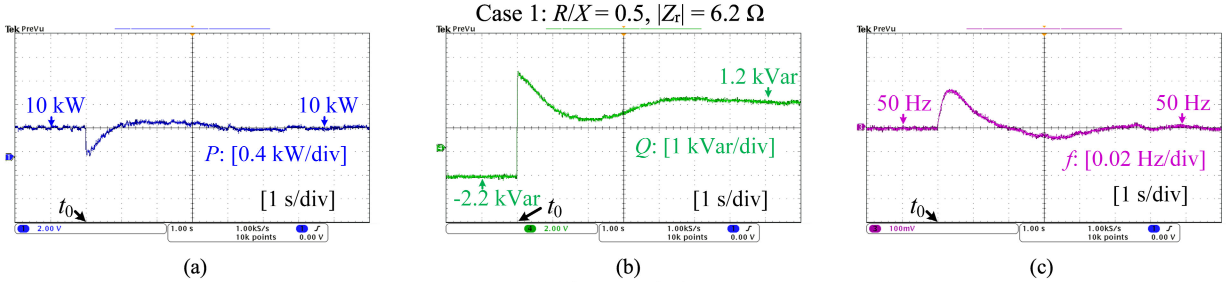

(a) (b) (c)

Case 1: $R/X = 0.5$, $|Z_r| = 6.5\ \Omega$

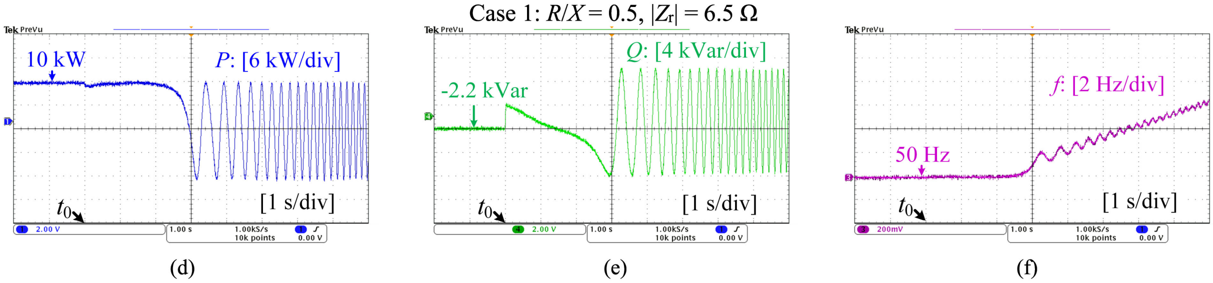

(d) (e) (f)

Fig. 12. Verification of Type-I large disturbance impedance boundaries (terminal voltage drops by 0.4 p.u. at t_0 and recovers at t_0+t_f): Case 1: $R/X = 0.5$ and $|Z_r| = 6.2\ \Omega$: (a) active power waveforms, (b) reactive power waveforms, and (c) frequency waveforms; Case 2: $R/X = 0.5$ and $|Z_r| = 6.5\ \Omega$: (d) active power waveforms, (e) reactive power waveforms, and (f) frequency waveforms.

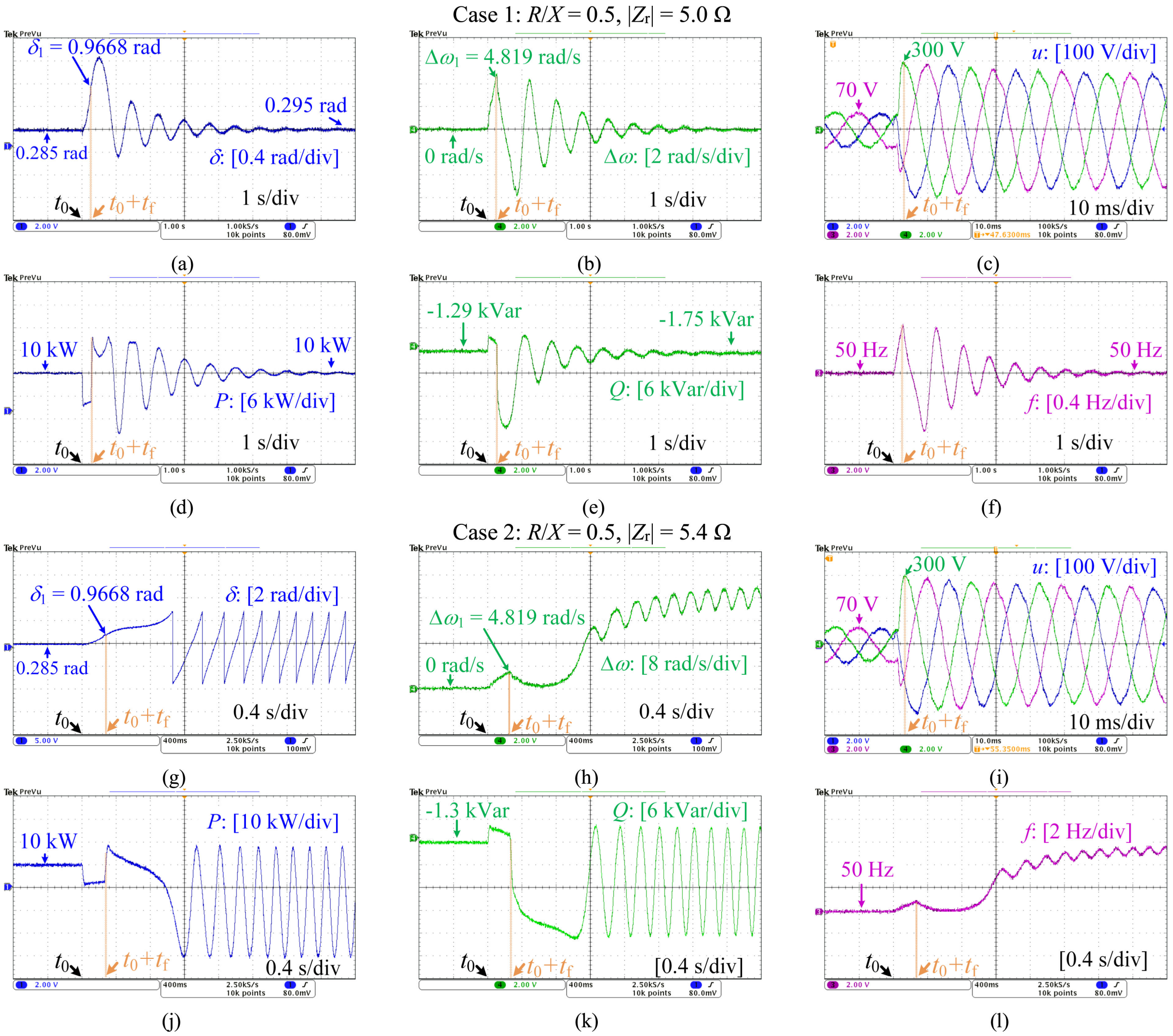

Fig. 13. Verification of impedance boundary for Type-II large disturbance (terminal voltage drops by 0.775 p.u. at t_0 and recovers at t_0+t_f): Case 1: $R/X = 0.5$ and $|Z_r| = 5.0\ \Omega$: (a) power angle, (b) angular frequency deviation, (c) terminal voltage, (d) active power, (e) reactive power, and (f) frequency waveforms; Case 2: $R/X = 0.5$, $|Z_r| = 5.4\ \Omega$: (g) power angle, (h) angular frequency deviation, (i) terminal voltage, (g) active power, (k) reactive power, and (l) frequency waveforms.

to oscillate continuously, and accordingly, the frequency also increases and diverges from the equilibrium point finally. The experimental results validate the high accuracy of the output impedance boundary for Type-I large-disturbance stability.

2) Type-II Large Disturbance: Then, the output impedance boundary for Type-II large disturbance stability, which is mathematically expressed by (32), is verified. Initially, the VSG system operates normally and steadily. The breaker is closed at t_0 and is open after t_f. A 0.775 p.u. sag of the terminal voltage is designed by letting k equal 3.125. D equals 15 p.u. The experimental waveforms are shown in Fig. 13. When the system detects the voltage recovery at $t_0 + t_f$, the measured power angle δ_1 and the angle frequency deviation $\Delta\omega_1$ are 0.9668 rad and 4.819 rad/s, respectively, as shown in Fig. 13(a) and (b). Substituting the observed values of δ_1 and $\Delta\omega_1$ into (14) can yield the corresponding output impedance boundary as illustrated in Fig. 14. It can be seen that the critical value of the output impedance is 5.05 Ω when $R/X = 0.5$. Accordingly, Case 1 ($|Z_r| = 5.0\ \Omega$, $R/X = 0.5$) and Case 2 ($|Z_r| = 5.4\ \Omega$, $R/X = 0.5$), which are located in and out of the stable region, respectively,

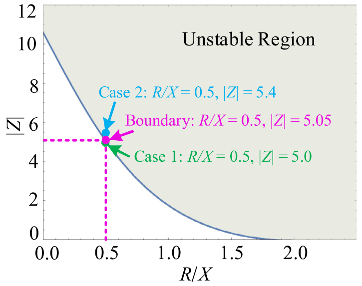

Fig. 14. Output impedance boundary for Type-II large disturbance in the case of Fig. 13.

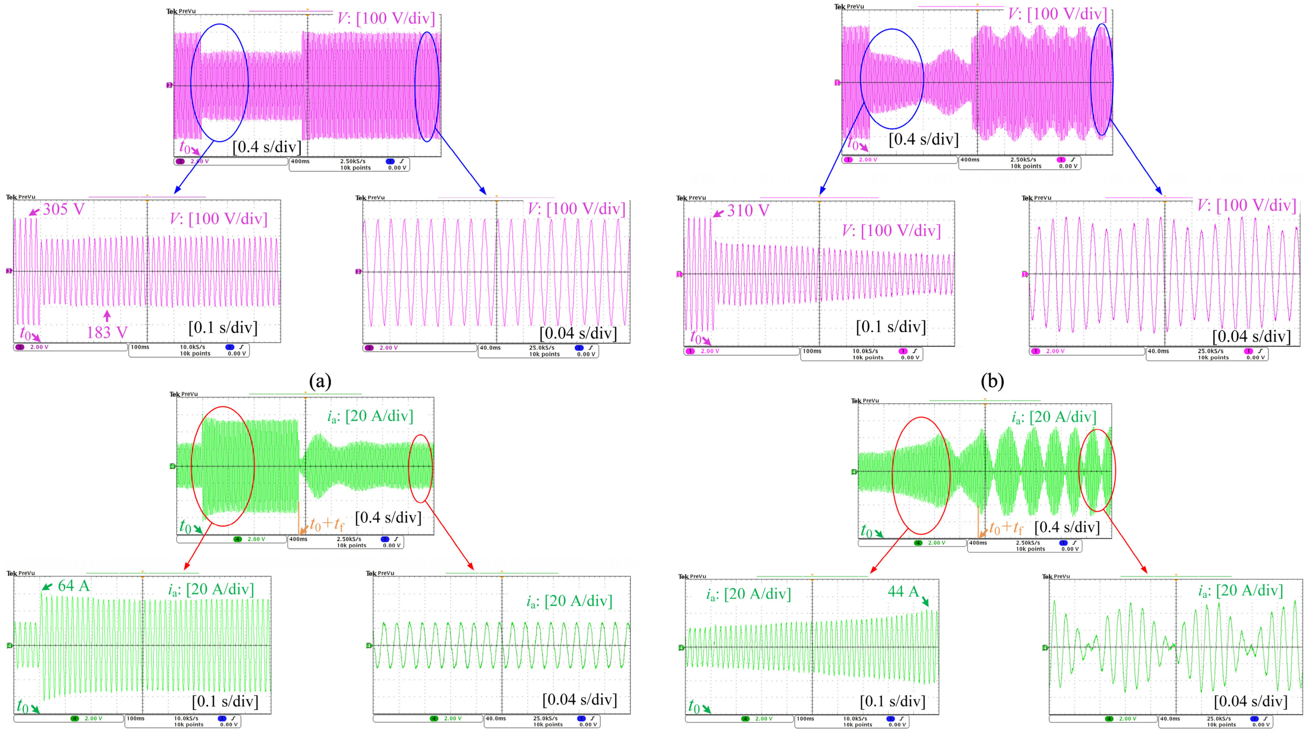

(a) (b) (c) (d)

Fig. 15. A-phase terminal voltage and A-phase current waveforms of the traditional fixed virtual impedance control in Scenario I (terminal voltage drops by 0.4 p.u. at t_0 and recovers at t_0+t_f): (a) and (c): $R_v = 1.48\ \Omega$ and $L_v = 4.7$ mH; (b) and (d): $R_v = 3\ \Omega$ and $L_v = 30$ mH.

are selected to verify the output impedance boundary described by (32).

The impedance value $|Z_r| = 5.0\ \Omega$ is very close to the critical value. Consequently, as shown in Fig. 13(d), there is a sag at the first overshoot of the active power waveform during the fault recovery process after $t_0 + t_f$, which indicates that the power angle has swung to the right side of the peak value of the power angle curve. If it exceeds the right equilibrium point, the system would lose stability. $|Z_r| = 5.0\ \Omega$ is opportunely located in the stable region; thus, the system returns to a steady-state point finally.

On the contrary, the impedance value $|Z_r| = 5.4\ \Omega$ is outside the stable region as shown in Fig. 14. Under this condition, the power angle passes over the equilibrium point on the right side and cannot swing back to the left side like the case of $|Z_r| = 5.0\ \Omega$, so the system gradually loses synchronization and becomes unstable, which can be observed from the experimental results shown in Fig. 13. Based on the experimental results, it can be proven that the output impedance boundary for Type-II large-disturbance stability exhibits nice accuracy.

D. Verification of the Proposed Large-Disturbance Stability Enhancement Strategy

Comparative experiments between the proposed adaptive virtual impedance strategy and traditional fixed virtual impedance control strategy are performed in this section to prove the superiority of the strategy proposed in Section V.

1) Scenario I: Type-I Large Disturbance: For Type-I large disturbance, according to (34), a 0.4 p.u. terminal voltage sag is designed by setting $k = 0.9625$ as the experimental case. As explained before, for the traditional fixed virtual impedance control in which the virtual impedance value does not change during the whole process, even if the virtual impedance value is well designed, the system will also face the problems of overcurrent or instability under large disturbances.

Fig. 15 shows the terminal voltage and output current waveforms of the VSG system with the traditional fixed virtual impedance control strategy. As shown in Fig. 15(c), although the smaller virtual impedance can ensure the stability of the system, the current is over the tolerance of the converter during the disturbance. However, it can be seen from Fig. 15(d) that a larger virtual impedance can restrict the current to the maximum limit of the inverter, yet the system is more liable to divergence and instability.

Under the same operation condition, using the proposed adaptive impedance control can solve the above problems. The experimental waveforms when using the proposed adaptive impedance control strategy are shown in Fig. 16, and Fig. 17 shows the adaptive virtual impedance curve during the large-disturbance process. At t_0, the breaker is closed and the terminal voltage drops by 0.4 p.u., and the virtual impedance quickly switches to Z_p, which is selected in the safe operating area and

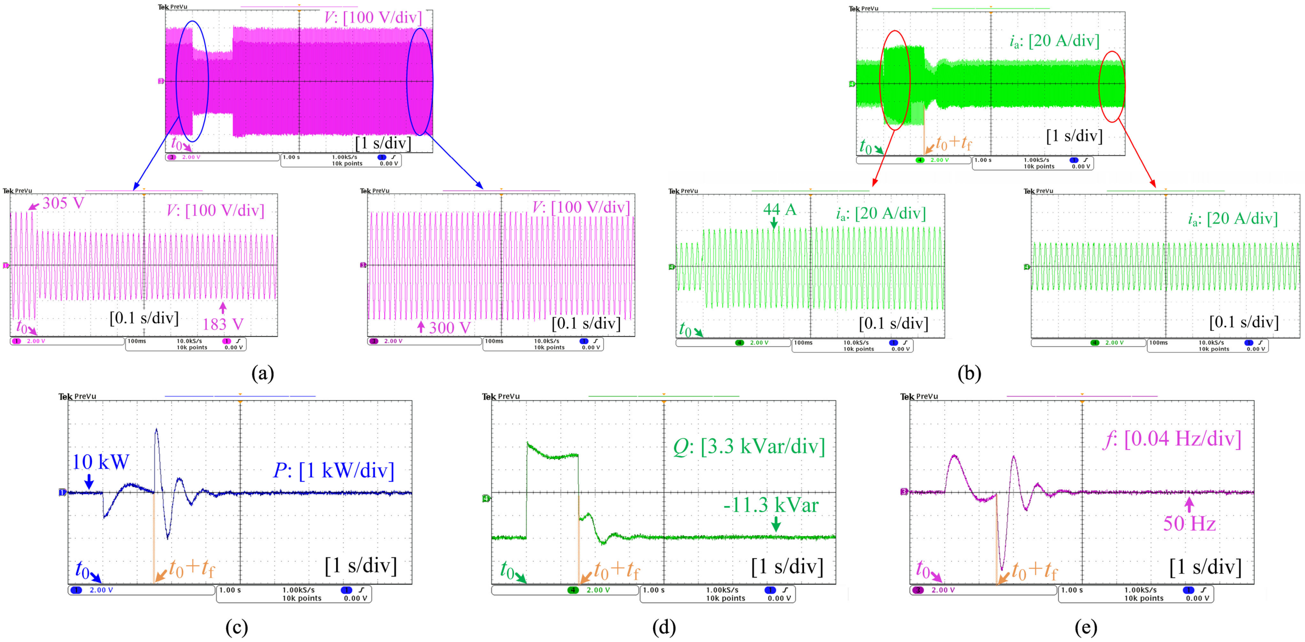

(a) (b) (c) (d) (e)

Fig. 16. Experimental waveforms of the proposed adaptive control strategy in Scenario I (terminal voltage drops by 0.4 p.u. at t_0 and recovers at t_0+t_f): (a) A-phase terminal voltage waveform, (b) A-phase current waveform, (c) active power waveform, (d) reactive power waveform, and (e) frequency waveform.

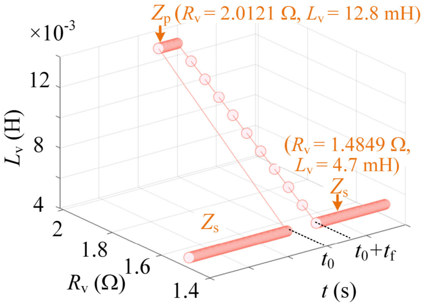

Fig. 17. Adaptive virtual impedance curve in Scenario I.

is used to limit the transient current and improve the stability of the system simultaneously. After t_f, the terminal voltage is recovered, and the virtual impedance is restored to the optimized steady-state impedance Z_s step by step by using a ramp control.

It can be observed from the terminal voltage, output current, active power, reactive power, and frequency waveforms shown in Fig. 16 that the system always maintains stability throughout the whole large disturbance, and meanwhile, the output current is always within the limited range. Besides, during the impedance switching process, the variations of the frequency are gentle.

2) Scenario II: Type-II Large Disturbance: Furthermore, a more serious case of 0.9 p.u. terminal voltage sag, which belongs to Type-II large disturbance, is designed by setting $k = 0.1$ in Fig. 9 to verify the Scenario II part of the proposed strategy.

As described before, the system stability will be highly affected by Type-II large disturbance when the traditional fixed virtual impedance control method is used. As shown in Fig. 18, under the first set of lesser virtual impedance values, the system can maintain stability but the overcurrent is more serious during the Type-II large disturbance. Under the second set of greater virtual impedance values, the current limitation can be guaranteed during the disturbance, yet the system becomes diverging and unstable. In this scenario, the traditional VSG strategy cannot work stably.

Fig. 19 gives the output waveforms of the VSG system with the proposed adaptive virtual impedance control strategy when the terminal voltage drops to 0.1 p.u., and the adaptive virtual impedance curve is as shown in Fig. 20. At t_0, the grid voltage sag occurs, and the virtual impedance quickly switches from Z_s, used for the steady state, to Z_f, chosen according to the current limiting boundary (29) for Stage II. After a duration of t_f, the grid voltage recovers, and the virtual impedance selects Z_r in the light of the boundaries (32) derived for Stage III. Finally, when the system reaches a steady state again, the virtual impedance is restored to the steady-state value Z_s via a ramp control and the system returns to normal operation before the disturbance.

The corresponding other results, viz., the terminal voltage, output current, active power, reactive power, and frequency waveforms, are shown in Fig. 19(a)–(e). The results show that the proposed strategy can solve the problems of overcurrent and power angle instability during the fault simultaneously, and help the system to ride through the large disturbance successfully. In addition, during the whole process, the frequency only exhibits a small variation. Compared with the traditional strategy, the proposed strategy can enhance the large-disturbance stability of VSG significantly.

As a whole, based on the above experimental verification, it can be concluded that the theoretical modeling and analysis results are accurate and the proposed strategy can enlarge the stability margin of VSG effectively.

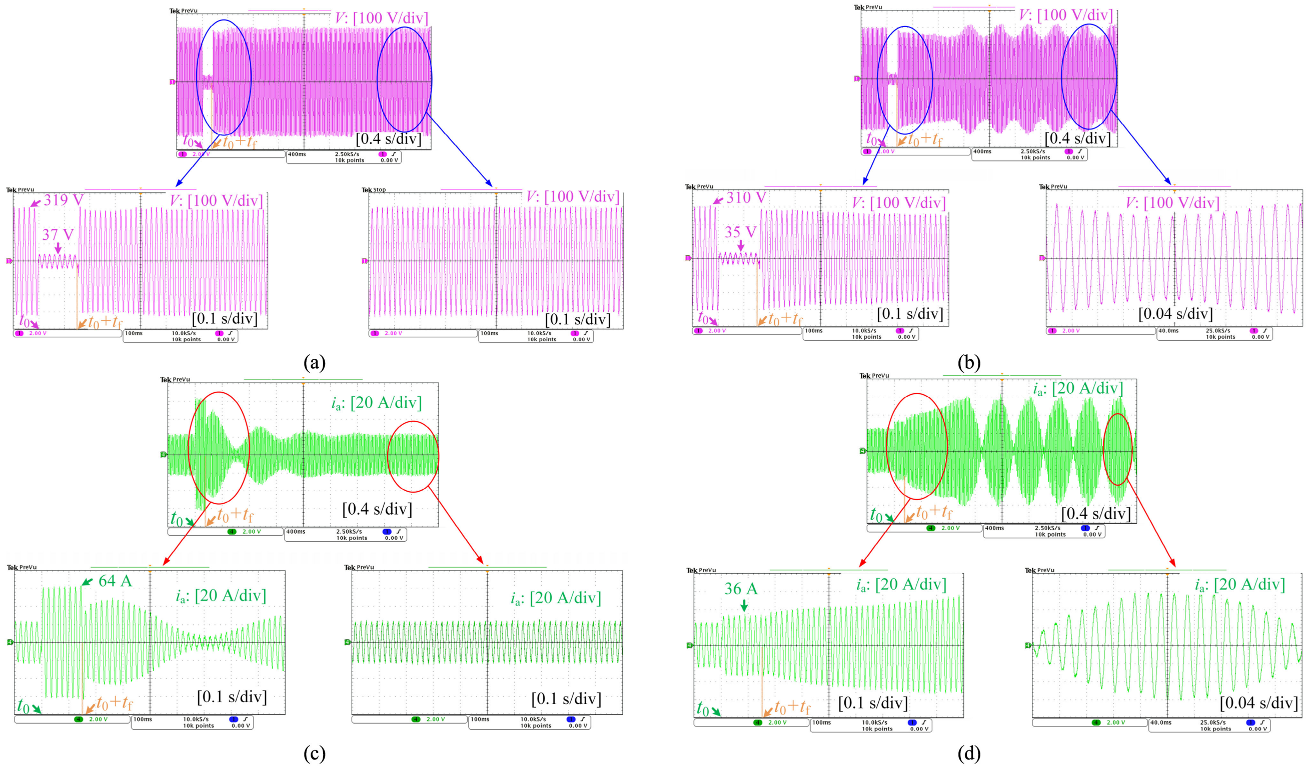

Fig. 18. A-phase terminal voltage and A-phase current waveforms of the traditional fixed virtual impedance control in Scenario II (a 0.9 p.u. terminal voltage sag occurs at t_0 and recovers at t_0+t_f). (a) and (c) $R_v = 1.45\ \Omega$ and $L_v = 13.9$ mH. (b) and (d) $R_v = 4.36\ \Omega$ and $L_v = 24.3$ mH.

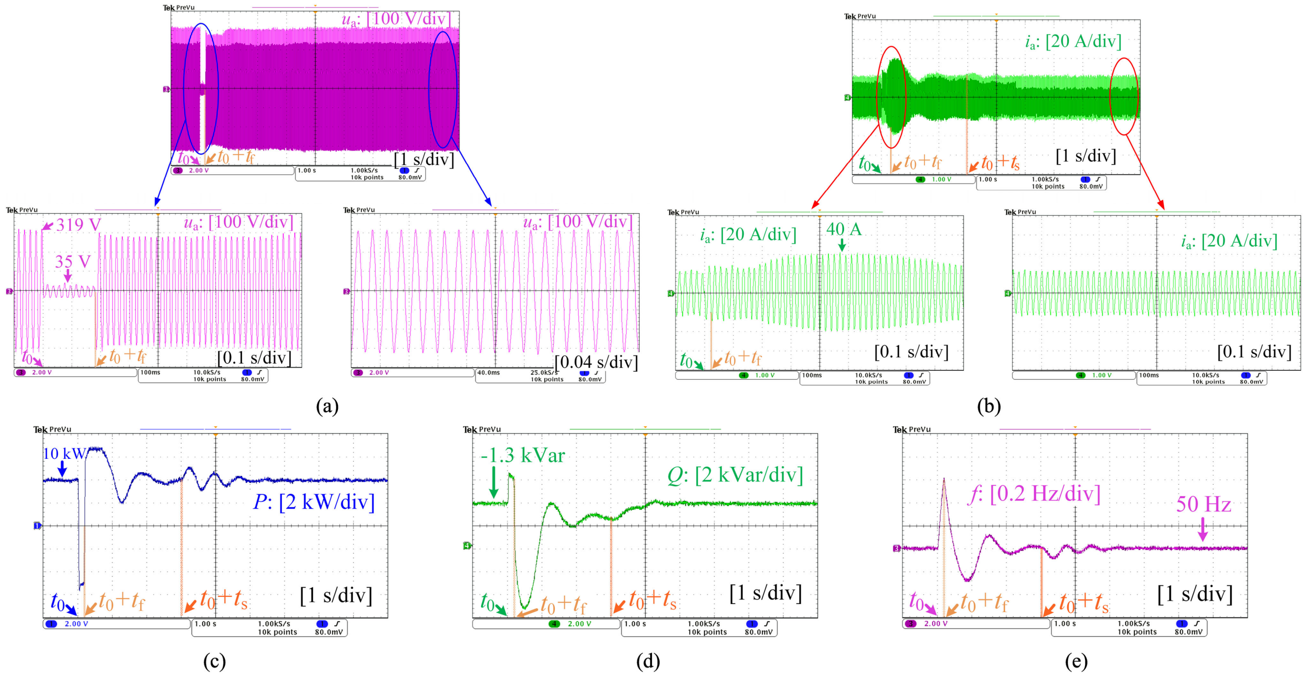

Fig. 19. Experimental waveforms of the proposed adaptive control strategy in Scenario II (a 0.9 p.u. terminal voltage sag occurs at t_0 and recovers at t_0+t_f). (a) A-phase terminal voltage, (b) A-phase current, (c) active power, (d) reactive power, and (e) frequency waveforms.

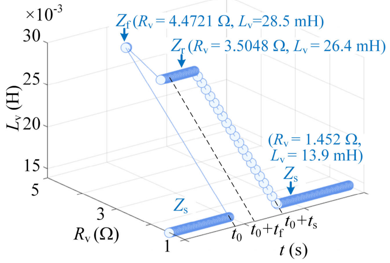

Fig. 20. Adaptive virtual impedance curve in Scenario II.

VII. CONCLUSION

In this article, novel output impedance design rules and control strategies for grid-connected VSG considering the enhancement of large-disturbance stability are presented. The large-disturbance stability problem involves two important issues, viz., the overcurrent issue during the electromagnetic transient process and the power angle stability issue during the electromechanical transient process. For the electromagnetic transient process, it is proved that the VFC-VSSI method exhibits the smallest peak current and the least settling time by the comparative analysis. The output impedance constraints for current limiting during the electromagnetic transient process are calculated. For the power angle stability, the cases are classified into two types to be addressed, respectively, according to whether there is an equilibrium point during the whole transient process. For the Type-I case, there still exists a shared impedance value that can satisfy the current limiting constraint and the Lyapunov stability condition simultaneously. Thereby, the shared output impedance stability region encircled by different stability boundaries is presented. For the Type-II case, the shared output impedance stability region does not exist anymore. Hence, the whole process is divided into three physical stages and then the output impedance boundaries for different stages are analyzed, respectively. Based on the proposed quantitative output impedance design rules, a large-disturbance stability enhancement method from the perspective of output impedance optimization is further proposed. Finally, the experimental results prove that the results of theoretical analysis are correct and the proposed strategy can effectively suppress the transient current and enlarge the stability region simultaneously under a large disturbance. In the future, the effects of reactive power control during the large-disturbance process will be considered further.

APPENDIX

A. *Derivation of the Output Impedances of CFC-VSSI and VFC-VCDI Structures*

As for the CFC-VSSI structure shown in Fig. 3(a), the voltage reference of the voltage loop can be described by

$$\begin{bmatrix} u^*_{d,\mathrm{CFC-VSSI}} \\ u^*_{q,\mathrm{CFC-VSSI}} \end{bmatrix} = \begin{bmatrix} e^*_d \\ e^*_q \end{bmatrix} - \begin{bmatrix} R_v & -X_v \\ X_v & R_v \end{bmatrix} \cdot \begin{bmatrix} i_{d,\mathrm{CFC-VSSI}} \\ i_{q,\mathrm{CFC-VSSI}} \end{bmatrix}. \tag{35}$$

The current reference of the current loop can be written as

$$\begin{bmatrix} i^*_{d,\mathrm{CFC-VSSI}} \\ i^*_{q,\mathrm{CFC-VSSI}} \end{bmatrix} = \begin{bmatrix} u^*_{d,\mathrm{CFC-VSSI}} - u_d \\ u^*_{q,\mathrm{CFC-VSSI}} - u_q \end{bmatrix} \cdot \left(k_{\mathrm{vp}} + \frac{k_{\mathrm{vi}}}{s} \right) \tag{36}$$

where k_{vp} and k_{vi} are the proportional and integral coefficients of the PI controller of the voltage loop.

Based on (6), (35), and (36), the output impedance can be obtained as

$$\begin{cases} Y_{dd,\mathrm{CFC-VSSI}} = \dfrac{G(s)G_u(s)[1+R_vG_u(s)G(s)]}{[1+R_vG(s)G_u(s)]^2+[X_vG(s)G_u(s)]^2} \\ Y_{dq,\mathrm{CFC-VSSI}} = \dfrac{X_vG_u(s)^2G(s)^2}{[1+R_vG(s)G_u(s)]^2+[X_vG(s)G_u(s)]^2} \end{cases} \tag{37}$$

where $G(s) = \frac{k_{\mathrm{cp}}s+k_{\mathrm{ci}}}{L_1s^2+(k_{\mathrm{cp}}+R_1)s+k_{\mathrm{ci}}}$ and $G_u(s) = \frac{k_{\mathrm{vp}}s+k_{\mathrm{vi}}}{s}$.

Regarding the VFC-VCDI structure in Fig. 3(c), the current reference becomes

$$\begin{cases} i^*_{d,\mathrm{VFC-VCDI}} = \dfrac{e_d-u_d+i_{q,\mathrm{VFC-VCDI}}\omega_sL_v}{R_v+sL_v} \\ i^*_{q,\mathrm{VFC-VCDI}} = \dfrac{e_q-u_q-i_{d,\mathrm{VFC-VCDI}}\omega_sL_v}{R_v+sL_v}. \end{cases} \tag{38}$$

With the same current control loop, which is mathematically expressed as (6), the output impedance of VFC-VCDI can be derived similarly according to (6) and (38), that is

$$\begin{cases} Y_{dd,\mathrm{VFC-VCDI}}(s) = \dfrac{G(s)\cdot(R_v+sL_v)}{[G(s)\cdot X_v]^2+(R_v+sL_v)^2} \\ Y_{qd,\mathrm{VFC-VCDI}}(s) = \dfrac{G(s)^2\cdot X_v}{[G(s)\cdot X_v]^2+(R_v+sL_v)^2} \end{cases} \tag{39}$$

where $G(s) = \frac{k_{\mathrm{cp}}s+k_{\mathrm{ci}}}{L_1s^2+(k_{\mathrm{cp}}+R_1)s+k_{\mathrm{ci}}}$.

B. *Demonstration of the Lyapunov function*

This section is to prove whether the function (22) satisfies the definition of Lyapunov function [16] as follows.

1) It has static points at the two equilibrium points of (21).
2) It is positive definite in the neighborhood of one of the equilibrium points.
3) Its derivative is not positive definite, viz., $\dot{V} \leq 0$.

First, the demonstration of condition 1) is given as follows:

$$\begin{aligned} \mathrm{grad}V &= \begin{bmatrix} \dfrac{\partial V}{\partial \Delta\omega} \\ \dfrac{\partial V}{\partial \delta} \end{bmatrix} = \begin{bmatrix} \dfrac{\partial E_{\mathrm{k}}}{\partial \Delta\omega} \\ \dfrac{\partial E_{\mathrm{p}}}{\partial \delta} \end{bmatrix} \\ &= \begin{bmatrix} M\Delta\omega \\ -\left(P_{\mathrm{m}} + \frac{3U^2\sin\varphi}{|Z|}\right) + \frac{3EU}{|Z|}\sin(\delta+\varphi) \end{bmatrix}. \end{aligned} \tag{40}$$

At the static point, the gradient equals 0, which means that the electromagnetic power equals the mechanical power. The two static points, which are also the equilibrium points of (21), can be obtained as

$$\delta_1 = \delta_0, \delta_2 = \pi - 2\varphi - \delta_0. \tag{41}$$

Condition 1) is proved.

Second, the demonstration of condition 2) is given by checking the Hessian matrix, which is written as

$$H = \begin{bmatrix} \frac{\partial^2 V}{\partial \Delta\omega^2} & \frac{\partial^2 V}{\partial \Delta\omega \partial \delta} \\ \frac{\partial^2 V}{\partial \Delta\omega \partial \delta} & \frac{\partial^2 V}{\partial \delta^2} \end{bmatrix} = \begin{bmatrix} M & 0 \\ 0 & \frac{3EU}{|Z|}\cos(\delta+\varphi) \end{bmatrix}. \tag{42}$$

According to Sylvester's theorem, when $M > 0$ (always true) and $3EU\cos(\delta+\varphi)/|Z| > 0$ (viz., $\delta + \varphi < \pi/2$), the Hessian matrix is positive definite. Obviously, the left equilibrium point δ_0 of (21) satisfies these conditions. Therefore, V is positive definite at δ_0. Condition 2) is proved.

Third, condition 3) is proved by analyzing its derivative. V represents the total energy of the whole system, and its derivative represents the dissipation speed of the energy. Calculating the derivative of E_k and E_p, respectively, gives

$$\begin{aligned} \frac{\mathrm{d}E_k}{\mathrm{d}t} &= \frac{\mathrm{d}E_k}{\mathrm{d}\omega}\frac{\mathrm{d}\omega}{\mathrm{d}t} = M\Delta\omega\frac{\mathrm{d}\Delta\omega}{\mathrm{d}t} = M\frac{\mathrm{d}\Delta\omega}{\mathrm{d}t}\cdot\Delta\omega \\ &= \left[P_m - \left(\frac{3EU}{|Z|}\sin(\delta+\varphi) - \frac{3U^2\sin\varphi}{|Z|}\right)\right]\Delta\omega \\ &\quad - D\Delta\omega^2 \end{aligned} \tag{43}$$

$$\begin{aligned} \frac{\mathrm{d}E_p}{\mathrm{d}t} &= \frac{\mathrm{d}E_p}{\mathrm{d}\delta}\frac{\mathrm{d}\delta}{\mathrm{d}t} \\ &= \left[-\left(P_m + \frac{3U^2\sin\varphi}{|Z|}\right) + \frac{3EU}{|Z|}\sin(\delta+\varphi)\right]\cdot\Delta\omega. \end{aligned} \tag{44}$$

Thus,

$$\dot{V} = \frac{\mathrm{d}V}{\mathrm{d}t} = \frac{\mathrm{d}E_k}{\mathrm{d}t} + \frac{\mathrm{d}E_p}{\mathrm{d}t} = -D\Delta\omega^2. \tag{45}$$

As can be seen from (45), $\dot{V} \leq 0$. Namely, $\dot{V}$ is not positive definite. Condition 3) is proved.

REFERENCES

[1] F. Blaabjerg, Z. Chen, and S. B. Kjaer, "Power electronics as efficient interface in dispersed power generation systems," *IEEE Trans. Power Electron.*, vol. 19, no. 5, pp. 1184–1194, Sep. 2004.

[2] I. Cvetkovic, D. Boroyevich, R. Burgos, L. Chi, M. Jaksic, and P. Mattavelli, "Modeling of a virtual synchronous machine-based grid-interface converter for renewable energy systems integration," in *Proc. IEEE 15th Workshop Control Model. Power Electron.*, 2014, pp. 1–7.

[3] H. Alatrash, A. Mensah, E. Mark, G. Haddad, and J. Enslin, "Generator emulation controls for photovoltaic inverters," *IEEE Trans. Smart Grid*, vol. 3, no. 2, pp. 996–1011, Jun. 2012.

[4] Q. Zhong and G. Weiss, "Synchronverters: Inverters that mimic synchronous generators," *IEEE Trans. Ind. Electron.*, vol. 58, no. 4, pp. 1259–1267, Apr. 2011.

[5] N. Pogaku, M. Prodanovic, and T. C. Green, "Modeling, analysis and testing of autonomous operation of an inverter-based microgrid," *IEEE Trans. Power Electron.*, vol. 22, no. 2, pp. 613–625, Mar. 2007.

[6] J. Sun, "Impedance-based stability criterion for grid-connected inverters," *IEEE Trans. Power Electron.*, vol. 26, no. 11, pp. 3075–3078, Nov. 2011.

[7] H. Wu *et al.*, "Small-signal modeling and parameters design for virtual synchronous generators," *IEEE Trans. Ind. Electron.*, vol. 63, no. 7, pp. 4292–4303, Jul. 2016.

[8] J. He and Y. W. Li, "Analysis, design, and implementation of virtual impedance for power electronics interfaced distributed generation," *IEEE Trans. Ind. Appl.*, vol. 47, no. 6, pp. 2525–2538, Nov./Dec. 2011.

[9] L. Zhang, L. Harnefors, and H. Nee, "Power-synchronization control of grid-connected voltage-source converters," *IEEE Trans. Power Syst.*, vol. 25, no. 2, pp. 809–820, May 2010.

[10] Ö. Göksu, R. Teodorescu, C. L. Bak, F. Iov, and P. C. Kjær, "Instability of wind turbine converters during current injection to low voltage grid faults and PLL frequency based stability solution," *IEEE Trans. Power Syst.*, vol. 29, no. 4, pp. 1683–1691, Jul. 2014.

[11] H. Xin, L. Huang, L. Zhang, Z. Wang, and J. Hu, "Synchronous instability mechanism of P-F droop-controlled voltage source converter caused by current saturation," *IEEE Trans. Power Syst.*, vol. 31, no. 6, pp. 5206–5207, Nov. 2016.

[12] X. Wang, M. G. Taul, H. Wu, Y. Liao, F. Blaabjerg, and L. Harnefors, "Grid-synchronization stability of converter-based resources—An overview," *IEEE Open J. Ind. Appl.*, vol. 1, pp. 115–134, Sep. 2020.

[13] L. Zhou *et al.*, "Harmonic current and inrush fault current coordinated suppression method for VSG under non-ideal grid condition," *IEEE Trans. Power Electron.*, vol. 36, no. 1, pp. 1030–1042, Jan. 2021.

[14] Z. Shuai, W. Huang, C. Shen, J. Ge, and Z. J. Shen, "Characteristics and restraining method of fast transient inrush fault currents in synchronverters," *IEEE Trans. Ind. Electron.*, vol. 64, no. 9, pp. 7487–7497, Sep. 2017.

[15] K. Shi, W. Song, P. Xu, R. Liu, Z. Fang, and Y. Ji, "Low-voltage ride-through control strategy for a virtual synchronous generator based on smooth switching," *IEEE Access*, vol. 6, pp. 2703–2711, 2018.

[16] J. Machowski, *Power System Dynamics—Stability and Control*. New York, NY, USA: Wiley, 2008, pp. 222–230.

[17] L. Huang, H. Xin, Z. Wang, L. Zhang, K. Wu, and J. Hu, "Transient stability analysis and control design of droop-controlled voltage source converters considering current limitation," *IEEE Trans. Smart Grid*, vol. 10, no. 1, pp. 578–591, Jan. 2019.

[18] L. Chen *et al.*, "Investigation of a modified flux-coupling-type SFCL for low-voltage ride-through fulfillment of a virtual synchronous generator," *IEEE Trans. Appl. Supercond.*, vol. 30, no. 4, Jun. 2020, Art. no. 5601006.

[19] Y. Li, W. Li, L. Guo, N. Jin, and F. Lu, "Current sensor-less virtual synchronous generator model predictive control based on sliding mode observer," *IEEE Access*, vol. 9, pp. 17898–17908, 2021.

[20] J. Jongudomkarn, J. Liu, and T. Ise, "Virtual synchronous generator control with reliable fault ride-through ability: A solution based on finite-set model predictive control," *IEEE J. Emerg. Sel. Topics Power Electron.*, vol. 8, no. 4, pp. 3811–3824, Dec. 2020.

[21] T. Qoria, F. Gruson, F. Colas, G. Denis, T. Prevost, and X. Guillaud, "Critical clearing time determination and enhancement of grid-forming converters embedding virtual impedance as current limitation algorithm," *IEEE J. Emerg. Sel. Topics Power Electron.*, vol. 8, no. 2, pp. 1050–1061, Jun. 2020.

[22] C. Glockler, D. Duckwitz, and F. Welck, "Virtual synchronous machine control with virtual resistor for enhanced short circuit capability," in *Proc. IEEE PES Innov. Smart Grid Technol. Conf. Europe*, 2017, pp. 1–6.

[23] K. Shi, H. Ye, P. Xu, D. Zhao, and L. Jiao, "Low-voltage ride through control strategy of virtual synchronous generator based on the analysis of excitation state," *IET Gener., Transmiss. Distrib.*, vol. 12, no. 9, pp. 2165–2172, May 2018.

[24] H. Geng, L. Liu, and R. Li, "Synchronization and reactive current support of PMSG-based wind farm during severe grid fault," *IEEE Trans. Sustain. Energy*, vol. 9, no. 4, pp. 1596–1604, Oct. 2018.

[25] J. Alipoor, Y. Miura, and T. Ise, "Power system stabilization using virtual synchronous generator with alternating moment of inertia," *IEEE J. Emerg. Sel. Topics Power Electron.*, vol. 3, no. 2, pp. 451–458, Jun. 2015.

[26] H. Wu and X. Wang, "Design-oriented transient stability analysis of grid-connected converters with power synchronization control," *IEEE Trans. Ind. Electron.*, vol. 66, no. 8, pp. 6473–6482, Aug. 2019.

[27] H. Wu and X. Wang, "Design-oriented transient stability analysis of PLL-synchronized voltage-source converters," *IEEE Trans. Power Electron.*, vol. 35, no. 4, pp. 3573–3589, Apr. 2020.

[28] D. Pan, X. Wang, F. Liu, and R. Shi, "Transient stability of voltage-source converters with grid-forming control: A design-oriented study," *IEEE J. Emerg. Sel. Topics Power Electron.*, vol. 8, no. 2, pp. 1019–1033, Jun. 2020.

[29] P. Hart and B. Lesieutre, "Energy function for a grid-tied, droop-controlled inverter," in *Proc. North Amer. Power Symp.*, 2014, pp. 1–6.

[30] Z. Shuai, C. Shen, X. Liu, Z. Li, and Z. J. Shen, "Transient angle stability of virtual synchronous generators using Lyapunov's direct method," *IEEE Trans. Smart Grid*, vol. 10, no. 4, pp. 4648–4661, Jul. 2019.

[31] X. Xiong, C. Wu, B. Hu, D. Pan, and F. Blaabjerg, "Transient damping method for improving the synchronization stability of virtual synchronous generators," *IEEE Trans. Power Electron.*, vol. 36, no. 7, pp. 7820–7831, Jul. 2021.

[32] H. Wu and X. Wang, "A mode-adaptive power-angle control method for transient stability enhancement of virtual synchronous generators," *IEEE J. Emerg. Sel. Topics Power Electron.*, vol. 8, no. 2, pp. 1034–1049, Jun. 2020.

[33] T. Shintai, Y. Miura, and T. Ise, "Oscillation damping of a distributed generator using a virtual synchronous generator," *IEEE Trans. Power Del.*, vol. 29, no. 2, pp. 668–676, Apr. 2014.

[34] J. Liu, Y. Miura, and T. Ise, "Comparison of dynamic characteristics between virtual synchronous generator and droop control in inverter-based distributed generators," *IEEE Trans. Power Electron.*, vol. 31, no. 5, pp. 3600–3611, May 2016.

[35] Q. Zhong, P. Nguyen, Z. Ma, and W. Sheng, "Self-synchronized synchronverters: Inverters without a dedicated synchronization unit," *IEEE Trans. Power Electron.*, vol. 29, no. 2, pp. 617–630, Feb. 2014.

[36] R. H. Lasseter, Z. Chen, and D. Pattabiraman, "Grid-forming inverters: A critical asset for the power grid," *IEEE J. Emerg. Sel. Topics Power Electron.*, vol. 8, no. 2, pp. 925–935, Jun. 2020.

[37] A. D. Paquette and D. M. Divan, "Virtual impedance current limiting for inverters in microgrids with synchronous generators," *IEEE Trans. Ind. Appl.*, vol. 51, no. 2, pp. 1630–1638, Mar./Apr. 2015.

[38] S. D'Arco, J. A. Suul, and O. B. Fosso, "Small-signal modeling and parametric sensitivity of a virtual synchronous machine in islanded operation," *Int. J. Elect. Power Energy Syst.*, vol. 72, pp. 3–15, Mar. 2015.

[39] M. Li, Y. Wang, Y. Liu, N. Xu, S. Shu, and W. Lei, "Enhanced power decoupling strategy for virtual synchronous generator," *IEEE Access*, vol. 8, pp. 73601–73613, Apr. 2020.

[40] Y. Chen, R. Hesse, D. Turschner, and H. Beck, "Comparison of methods for implementing virtual synchronous machine on inverters," in *Proc. Int. Conf. Renewable Energies Power Qual.*, 2012, pp. 1–6.

[41] X. Liang, C. Andalib-Bin-Karim, W. Li, M. Mitolo, and M. N. S. K. Shabbir, "Adaptive virtual impedance-based reactive power sharing in virtual synchronous generator controlled microgrids," *IEEE Trans. Ind. Appl.*, vol. 57, no. 1, pp. 46–60, Jan./Feb. 2021.

[42] Y. Li, Y. Gu, Y. Zhu, A. Junyent-Ferré, X. Xiang, and T. C. Green, "Impedance circuit model of grid-forming inverter: Visualizing control algorithms as circuit elements," *IEEE Trans. Power Electron.*, vol. 36, no. 3, pp. 3377–3395, Mar. 2021.

[43] Y. Gu, Y. Li, Y. Zhu, and T. C. Green, "Impedance-based whole-system modeling for a composite grid via embedding of frame dynamics," *IEEE Trans. Power Syst.*, vol. 36, no. 1, pp. 336–345, Jan. 2021.

[44] A. R. Bergen, *Power Systems Analysis*. Englewood Cliffs, NJ, USA: Prentice-Hall, 1986.

Mingxuan Li (Member, IEEE) received the Ph.D. degree in electrical engineering from Xi'an Jiaotong University, Xi'an, China, in 2020.

From 2017 to 2019, he was a Visiting Scholar with the Department of Energy Technology, Aalborg University, Aalborg, Denmark. He is currently a Postdoctoral Researcher in control science and engineering with the University of Electronic Science and Technology of China, Chengdu, China. His research interests include distributed power generation systems, microgrids, stability analysis and control of converter-based systems, and artificial intelligence in modern power systems.

Sirui Shu received the B.S. degree in electrical engineering in 2019 from Xi'an Jiaotong University, Xi'an, China, where she is currently working toward the M.S. degree in electrical engineering.

Her research interests include the modeling and control of converters, and renewable energy integration.

Yue Wang (Member, IEEE) was born in Liaoning, China, in 1972. He received the B.S. degree from Xi'an Jiaotong University, Xi'an, China, in 1994, the M.S. degree from Beijing Jiaotong University, Beijing, China, in 2000, and the Ph.D. degree from Xi'an Jiaotong University, Xi'an, China, in 2003, all in electrical engineering.

He is currently a Full Professor with the School of Electrical Engineering, Xi'an Jiaotong University. His research interests include wireless power transfer, active power filters, multilevel converters, and HVdc.

Peng Yu received the B.S. degree in electrical engineering from Guangxi University, Nanning, China, in 2017. He is currently working toward the M.S. degree in electrical engineering with Xi'an Jiaotong University, Xi'an, China.

His research interests include the modeling and control of converters, and renewable energy integration.

Yonghui Liu (Member, IEEE) received the B.S. degree from the Harbin Institute of Technology, Harbin, China, in 2013, and the M.S. degree from Xi'an Jiaotong University, Xi'an, China, in 2016, both in electrical engineering. She is currently working toward the joint Ph.D. degree in electrical engineering with Xi'an Jiaotong University, Xi'an, China, and Hong Kong Polytechnic University, Hong Kong.

Her research interests include modeling and control of converters, renewable energy integration, VSC-HVdc, and wireless power transfer.

Zhenyuan Zhang (Senior Member, IEEE) received the B.S. degree from Chang'an University, Xi'an, China, in 2007, and the Ph.D. degree from the University of Texas at Arlington, Arlington, TX, USA, in 2015, both in electrical engineering.

He is currently a Professor with the School of Mechanical and Electrical Engineering, University of Electronic Science and Technology of China, Chengdu, China. Since 2010, he has been the Project Associate with IEEE/NFPA Arc Flash Research Project. His research interests include smart grids and arc flash research, but he has also been involved in power system analysis, renewable energy, electrical safety analysis, and power market researches.

Weihao Hu (Senior Member, IEEE) received the B.Eng. and M.Sc. degrees from Xi'an Jiaotong University, Xi'an, China, in 2004 and 2007, respectively, both in electrical engineering, and the Ph.D. degree from Aalborg University, Aalborg, Denmark, in 2012.

He is currently a Full Professor and the Director of Institute of Smart Power and Energy Systems, University of Electronics Science and Technology of China, Chengdu, China. He was an Associate Professor with the Department of Energy Technology, Aalborg University, Aalborg, Denmark, and the Vice Program Leader of Wind Power System Research Program with the same department. His research interests include artificial intelligence in modern power systems and renewable power generation. He has led/participated in more than 15 national and international research projects and he has more than 170 publications in his technical field.

Prof. Hu is an Associate Editor for the *IET Renewable Power Generation*, a Guest Editor-in-Chief for the *Journal of Modern Power Systems*, and Clean Energy Special Issue on Applications of Artificial Intelligence in Modern Power Systems, a Guest Editor-in-Chief for the Transactions of China Electrical Technology Special Issue on Planning and operation of multiple renewable energy complementary power generation systems, and a Guest Editor for the IEEE TRANSACTIONS ON POWER SYSTEMS Special Section on enabling very high penetration renewable energy integration into future power systems. He was serving as the Technical Program Chair for IEEE Innovative Smart Grid Technologies Asia 2019 and is serving as the Conference Chair for the Asia Energy and Electrical Engineering Symposium. He is currently serving as the Chair of IEEE Chengdu Section PELS Chapter. He is a Fellow of the Institution of Engineering and Technology, London, U.K.

Frede Blaabjerg (Fellow, IEEE) received the Ph.D. degree in electrical engineering from Aalborg University, Aalborg, Denmark, in 1995.

He was with ABB-Scandia, Randers, Denmark, from 1987 to 1988. He became an Assistant Professor in 1992, an Associate Professor in 1996, and a Full Professor of power electronics and drives in 1998. From 2017, he became a Villum Investigator. He is an Honoris Causa with University Politehnica Timisoara, Romania, and Tallinn Technical University, Estonia. His research interests include power electronics and its applications, such as in wind turbines, PV systems, reliability, harmonics, and adjustable speed drives. He has authored/coauthored more than 600 journal papers in the fields of power electronics and its applications. He has coauthored four monographs and editor of 10 books in power electronics and its applications.

Prof. Blaabjerg was the recipient of 32 IEEE Prize Paper Awards, the IEEE PELS Distinguished Service Award in 2009, the EPE-PEMC Council Award in 2010, the IEEE William E. Newell Power Electronics Award 2014, the Villum Kann Rasmussen Research Award 2014, the Global Energy Prize in 2019, and the 2020 IEEE Edison Medal. He was the Editor-in-Chief for the IEEE TRANSACTIONS ON POWER ELECTRONICS from 2006 to 2012. He has been a Distinguished Lecturer for the IEEE Power Electronics Society from 2005 to 2007 and for the IEEE Industry Applications Society from 2010 to 2011 as well as 2017 to 2018. In 2019–2020, he serves as the President of IEEE Power Electronics Society. He is the Vice-President of the Danish Academy of Technical Sciences too. He is nominated in 2014–2019 by Thomson Reuters to be between the most 250 cited researchers in Engineering in the world.